博士論文　　（要約）

DEVELOPMENT OF DIGITAL ANIMAL DOUBLE-PHOTON EMISSION TOMOGRAPHY USING TIME-OVER-THRESHOLD METHOD

(高分解能 PET 用新規 DOI 検出手法に関する研究)

チョガディ　モハンマド　アミン

(Mohammad Amin CHOGHADI)

The abridged dissertation submitted in partial fulfillment for the

degree of

Doctor of Philosophy in Engineering

Department of Bioengineering

Graduate School of Engineering

by M. Amin CHOGHADI

Supervisor: Professor Hiroyuki TAKAHASHI

August 2020

For my family and country that I did not have a chance to visit

during this work.

Abstract

In double-photon emission tomography (DPET), electronic readout plays an influential role in the detection efficiency as well as time resolution. Particularly in positron emission tomography (PET), due to the large number of detectors, a fast and efficient readout scheme is mandatory in order to reduce the number of cables while maintaining the detection efficiency and avoiding distortion in localizing the detection position. This will be of more importance for high-resolution PET imaging where finer detector pitch is used. Meanwhile, a predominant challenge in high-resolution PET imaging is resolving parallax error for which several depth-of-interaction (DOI) identification methods are proposed. Among all, dual-ended individual readout with pixelated arrays has been proved to be capable of good DOI performance.

The goal of this research is to develop an effective readout system for a 1.36-mm detector-pitch animal PET for sub-millimeter-resolution imaging. $1.2 \times 1.2 \times 20$ mm^3 Ce:GAGG crystal will be used in a modular configuration with individual coupling and dual-ended readout for DOI identification to remove parallax error. Dual-ended readout scheme for DOI accentuates the need for fast and efficient electronic readout that avoids loss or overlap of data. To provide such a system, a fully digital readout scheme based on the time-over-threshold (ToT) method was designed and assembled. In the first step, this

system was designed based on the conventional ToT method and tested for a 2-mm PET system in order to be evaluated in comparison with previous results. A **1-mm spatial resolution** was achieved for this animal PET scanner with acceptable energy and time resolution. The proposed method has no positioning distortion and could be applied to a 1.36-mm detector-pitch system once the crystal arrays are prepared.

Since the dual-ended method is based on the contrast between the energy of the output signals, unlike the 2-mm system, energy preservation capability of the readout method is important. The conventional ToT method does not show a good energy response and it should be modified to be applied to the DOI-PET system. A modified ToT approach is the dynamic ToT method that has a linear response over a wide range of energies. This was tested for a collimator-based double photon emission computed tomography (DPECT). The system showed an excellent energy response in a way that even X-ray emission of the ^{111}In source was extracted.

Acknowledgment

Table of Contents

6

List of Figures

8

List of Tables

1. INTRODUCTION

Gamma-ray imaging is a very common tool in nuclear medicine, and it has been developed in various methods that all can be categorized into two general methodologies; single-photon emission measurement, and double-photon emission (coincidence) measurement. Gamma camera (Anger camera) and single-photon emission computed tomography (SPECT) are examples of the first method where a variety of techniques including coded aperture masks [1] and parallel-hole collimators [2] are introduced. On the other hand, double-photon emission measurement is the principle of positron emission tomography (PET) which is widely used in nuclear medicine. It shows a very high sensitivity compared with SPECT since in SPECT a large portion of radiated photons is rejected by the collimator. In addition, PET also shows a very high signal-to-background ratio (SBR) since the detection system relies on a coincidence signal where two detectors identify the event. The coincidence signal can highly restrict the target event when the system has a very short time window for the coincidence. As a result, a high SBR is realized. The coincidence detection technique can be also applied to nuclides which emit two γ photons in a very short time [3]. This is the basic idea of double photon emission computed tomography (DPECT) [4]. In this work, both PET and DPECT are categorized as double photon emission tomography (DPET).

1.1.   Background

In DPET imaging, and more particularly in PET, electronic readout plays a significant role in the whole performance of the system including spatial resolution. The optimum spatial resolution can be achieved by using pixelated crystal arrays coupled individually to a photomultiplier tube (PMT) with independent electronic readout [5–7]. In recent advancements in detector design, detector pitch has been narrowed down to 0.5 mm [8, 9]. This means, within the same size of the gantry, the number of channels has greatly increased due to the finer detector pitch.

Even though spatial resolution can be improved by using detectors with finer pitch, it remains non-uniform due to parallax error which will be explained in detail in Chapter 5. Parallax error becomes more severe for systems with finer pitch and it must be cured if sub-millimeter imaging is the purpose. Several methods including dual-ended readout, use of multilayer crystals, 3D pixelated array of crystals, and use of monolithic block crystal with pixelated photosensors have been introduced to remove or reduce parallax error. Among all, dual-ended readout with pixelated crystals has gained attention in recent years [8–14]. A thorough study on dual-ended method was done in this research to make a right choice of crystal preparation for a sub-mm-resolution digital animal PET. Even though the results of this work show outstanding depth of interaction resolution, applying dual-ended method doubles the number of output channels. Consequently, in order to have an individual readout for each channel, a large number of cables and data acquisition ports are needed to transfer and record the signals.

In conventional PET systems, all channels of a PMT array are connected through a charge-division resistive network for multiplexing [15–19] in order to reduce the number of output cables. However, this analog method is associated with position distortion [15]

when recorded signals are demultiplexed even though some algorithms are proposed to reduce this distortion [20, 21]. Another disadvantage is that this resistive network increases the time constant of the output signals which leads to data overlap and lower detection efficiency [16, 18]. These drawbacks altogether result in a non-zero factor that degrades spatial resolution in the case of electronic encoding [5–7].

Another part of the electronic readout system is the analog-to-digital conversion (ADC) unit. In conventional ADC methods, the signal is digitized based on its amplitude. Depending on how many levels, the output is a number of bits (typically 12 bits) [22, 23] each of which needs a separate cable to be transferred. This again increases the number of cables and ports which is not desirable. Recently, the time-over-threshold (ToT) method has been investigated and applied to PET systems since it has a very simple concept and thus a compact electronic design [24–29]. ToT combines both ADC for energy measurement and time-to-digital conversion (TDC) for time resolution which is essential in time-of-flight (TOF) PET systems [30]. ToT method has undergone novel advancements to improve energy resolution and timing resolution in the past decade [30–35]; nonetheless, the basic idea is to record the duration of the signal when its absolute current or voltage is larger than a predefined threshold value. Since the digital output has binary amplitude – 0 for when there is no signal and 1 for when the signal is over the threshold – only one-bit signal and thereby one cable or connection is required. This, together with the compact architecture design of front-end application-specific integrated circuit (ASIC) boards, enables individual channel readout and digital multiplexing without increasing the number of cables and ports. The great advantage of this method is that multiplexing can be carried out digitally after ADC, which is completely distortion-free. In addition, since there is no resistive network anymore, there is no excessive time

constant in the output signal, which prevents data overlap and preserves detection efficiency.

In PET, energy resolution is not really a concern since only 511-keV gamma photons are emitted. However, in DPECT, nuclides emit different photon energies. For instance, ^{111}In emits a pair of 171 keV and 245 keV within 85 ns secondary emission half-life. In this case, energy resolution is of a great importance. Normal ToT method does not provide linear energy response and thereby it degrades the energy resolution of the system. Therefore, another scheme must be considered. Dynamic ToT method [31] has more linearity over a wide range of energies. Thereby, it was used in collimator-based digital DPECT development.

1.2.   Objective of Research

The purpose of this study is to develop a ToT-based full digital readout system for a high-resolution small animal PET system. As discussed before, for sub-millimeter spatial resolution, detector pitch must be reduced which results in an increased number of channels. In the first stage, a 2-mm detector-pitch animal PET scanner was developed with 8 modules of 12×12 array in a ring of 70mm diameter, with a total of 1152 channels, and performance of the readout system was evaluated. In the next system development, the detector pitch is 1.36 mm. To assemble a system with the same dimensions as of the 1.98-mm system, the number of detectors will be almost twice. The multiplexing distortion is more severe for detectors with smaller pitch if conventional method is used. In addition, since the pitch is smaller, parallax error increases. Dual-ended readout is the most effective approach to remove parallax error. However, applying this method doubles the number of output channels. In a nutshell, the next generation consists of 8 dual-ended

modules of 16 × 16 array, giving a total of 4096 output channels (~ 4 times the number of outputs in 1.98mm system). Therefore, the ToT-based digital readout system is more essential to process this large number of channels.

On the other hand, normal ToT method does not conserve the energy resolution of detectors that is quite important in the case of dual-ended readout for DOI estimation. Therefore, dynamic ToT method should be considered for future system developments. As a part of this study, a prototype of DPECT with a focused collimator was developed and tested with a dynamic ToT method. In DPECT, the energy resolution is of great importance since photons with different energies are emitted. Th dynamic ToT method provides a more linear energy response and preserves the energy resolution of the detector [31], which makes it the right choice for the DPECT system.

1.3. Summary of Results

A 1.98-mm system with a normal ToT method was assembled, and the system performance was evaluated. **1mm spatial resolution** was achieved in the center of the ring, which conforms to the theoretical value.

The DPECT system with a dynamic ToT readout provides very good energy resolution. However, further optimization of the collimator as well as increasing the number of detector modules is necessary to increase the coincidence count rate and achieve better images.

1.4. Outline of Thesis

In Chapter 2, the basic physics of radiation is introduced as a reference, and an overview of gamma imaging modalities in medicine is provided. In Chapter 3, basic

principle of PET imaging, detectors, and data processing is presented. Chapter 4 presents system development and evaluation of full digital readout method for 2-mm-pitch PET system. The influence of readout system on the spatial resolution of PET is discussed first, with the disadvantages and issues in conventional readout systems. It is explained that how ToT method could resolve those issues and facilitate the full-digital individual readout scheme. In Chapter 5, it is explained why parallax error is more severe and thus DOI identification is more essential for 1.36-mm-pitch system and common DOI identification approaches are presented. Chapter 6 describes the new DPET concept. At last, Chapter 7 summarizes the whole research with a conclusion and future direction for further advancement in the field.

2. BASIC PHYSICS OF RADIATION

2.1. Ionizing Radiation

Radiation can be categorized into electromagnetic radiation – including light, radiofrequency waves used in telecommunications, x-rays, and γ-rays – and particle radiation including α, β⁻, β⁺ and neutron radiation. These can be also categorized into ionizing and non-ionizing radiation. Ionizing radiation refers to radiation with energy high enough to remove electrons from atoms and ionize the matter [36]. This only occurs in the cases of high-energy electromagnetic waves; i.e. x-rays and γ-rays, and particle radiation (in the case of neutron radiation, ionization is indirect and is the subsequent process of radiation, for example, due to emission of γ photons). Another classification is charged and uncharged radiation [37]. α, β⁻, and β⁺ are charged radiation, and electromagnetic waves (including x and γ) and neutron rays are uncharged radiation.

2.2. Radioactive Decay

Some nuclei are unstable due to existing of excessive neutrons or protons. Such nuclei are disintegrated into more stable ones by emitting particles or high energy photons. This process is called radioactive decay which is a random process [36–40]. Activity for a radionuclide sample is defined as the rate of decay:

$$A \equiv -\frac{dN}{dt} = \lambda N \tag{2.1}$$

Where N is the number of atoms in the sample at time t, and λ is the decay constant. Considering N_0 atoms in the sample at $t = 0$, activity at $t = 0$ is $A_0 = \lambda N_0$, and activity at any time can be given by:

$$A(t) = A_0 e^{-\lambda t} \tag{2.2}$$

A common parameter to describe radioactivity is half-life defined as the time when the activity is reduced to half of the initial activity. It can be obtained from (2.2):

$$t_{1/2} = \frac{\ln 2}{\lambda} \tag{2.3}$$

In medical applications, since radiopharmaceuticals are naturally excreted from the body through biological processes [38], a biological decay constant λ_b with half-life T_b is also considered. In this case, effective decay constant λ_e and effective half-life T_e are calculated as follows:

$$\lambda_e = \lambda_p + \lambda_b \tag{2.4}$$

$$T_e = \frac{T_p \times T_b}{T_p + T_b} \tag{2.5}$$

where index "p" denotes physical decay of radiopharmaceutical.

There are several radioactive decay modes, namely nuclear fission, α-decay, β⁻-decay, β⁺-decay, electron capture, and isomeric transition. Nuclear fission is the process of spontaneous disintegration of a very heavy nucleus into two daughter nuclei. It is rarely used in nuclear medicine, merely ^{99}Mo that is the fission product of ^{235}U and used as technetium generator for ^{99m}Tc used in medical imaging. α particle has a very short range in the matter, *e.g.* about 0.03 mm in human tissue [38] and therefore it is not useful for

imaging, but there are therapy applications [41, 42].

β^- is a negatively charged particle with the same mass of an electron, typically emitted by neutron-rich nuclides. In this decay mode, a neutron disintegrates into a proton, β^- particle, and an antineutrino. While the daughter proton stays in the nucleus, β^-, and antineutrino are emitted out.

$$n \rightarrow p + \beta^- + \bar{\nu} + energy \qquad (2.6)$$

In some cases, the daughter nucleus is in an excited or metastable state, which undergoes the isomeric transition by emitting γ photons. This happens, for example, in the case of ^{133}Xe which produces ^{133}Cs in one of its three different excited states [39]. ^{90}Sr and its decay product, ^{90}Y, are both β^--emitters that are used in radiation therapies [43–46].

Positron emission (β^+-decay)

This decay mode is common in proton-rich radionuclides and is the basis of positron emission tomography. A proton turns into a neutron and emits a neutrino and a positively charged particle with the same mass of an electron, called positron (β^+).

$$transition\ energy + p \rightarrow n + \beta^+ + \nu + energy \qquad (2.7)$$
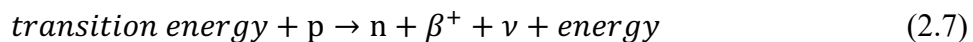
Since the mass of a neutron is one electron mass heavier than a proton, the radionuclide must have a transition energy level at least equivalent to the mass of two electrons (= 1.022 MeV) to undergo this disintegration. The excess transition energy from 1.022 MeV will be in the form of the kinetic energy of the produced positron and neutrino [38, 39]. Following is an example which is widely used in PET imaging:

$$^{18}_{9}\text{F} \rightarrow {}^{18}_{8}\text{O} + \beta^+ + \nu + energy \qquad (2.8)$$

Emitted positron soon combines with an electron (annihilation), and two 511-keV γ photons are emitted in opposite directions, making intrinsic collimation for coincidence detection. Same as β^--decay, in some cases the product nucleus is in an excited or metastable state and subsequent γ photons are emitted through isomeric transition [39].

Electron capture

There are cases where a proton-rich radionuclide cannot provide the needed transition energy for positron emission (1.022 MeV) as discussed above. In such cases, the nuclide captures an electron from the nearest electron shell. This electron combines with a proton, which results in the production of a neutron and emission of a neutrino [38].

$$p + e^- \rightarrow n + \nu + energy \qquad (2.9)$$

In cases where the nuclide has transition energy more than 1.022 MeV both EC and β^+-decay are possible [38, 39]. $^{111}_{49}I$, widely used in SPECT imaging, undergo electron capture:

$$^{111}_{49}I \xrightarrow{\text{EC}} {}^{111}_{48}Cd + \nu \qquad (2.10)$$

The initial transition energy appears in the form of the kinetic energy of the neutrino as well as characteristic X-ray and Auger electrons [39]. The latter two are emitted subsequently by the daughter product because there is a vacancy in the nearest electron shell. In addition, the daughter nuclide is often left in an excited or metastable state and consequently, γ photons are also emitted following the electron capture [39]. In the case of $^{111}_{49}I$, two subsequent γ photons with 171 keV and 245 keV are emitted, which makes this radionuclide applicable in SPECT. Since there is a correlation between these two γ emissions, i.e. both are emitted from one nucleus, this radionuclide can be used in DPECT which will be discussed in chapter 6.

Isomeric transition

Isomeric states are different energy states of a radionuclide. The nuclide may exist in an excited state, which emits γ photons so that it transits to its ground state. When an excited state of a nuclide has a long lifetime (more than a few minutes) it is called the metastable state and represented by symbol "m". ^{99m}Tc that is widely used in nuclear medicine, undergoes this decay mode:

$$^{99m}_{43}\text{Tc} \rightarrow\ ^{99}_{43}\text{Tc} + \gamma \tag{2.11}$$

2.3.   Interaction of Radiation with Matter

2.3.1. Charged-Particles Interactions

Unlike neutrons, charged particles are prone to interact with orbital electrons of an atom in the matter and remove them, which ionizes the atom. α particles are massive and move in a straight path until it loses its kinetic energy and captures two electrons consecutively to form a neutral He atom [47]. On the other hand, β^- and β^+ particles have very light mass and thereby interact more often with orbital electrons and undergo a lot of deflections. Therefore, these particles typically have a short penetrating range in the matter. This is in fact a good behavior in case of PET imaging. In PET, the pair of γ photons emitted following the annihilation of a positron and an electron are detected; therefore, the shorter positron range results in more accuracy in the image.

2.3.2. Interaction of Ionizing Photons with Matter

High-energy photons interact with matter through four major mechanisms including photoelectric effect, Compton scattering, pair production, and coherent (Rayleigh) scattering [36, 38, 47–49].

Photoelectric effect

The photoelectric effect is an interaction mechanism where the whole energy of the high-energy photon is absorbed by an electron, usually in K-shell orbital, resulting in the ejection of that electron from the atom. The electron is termed as "photoelectron" and has the kinetic energy E_{phe} after being ejected from the atom: If we notate the energy of γ photon and the binding energy of the electron as E_γ and E_B, respectively, then for E_{phe} we have:

$$E_{phe} = E_\gamma - E_B \qquad\qquad (2.12)$$

where E_γ and E_B are the energy of γ photon and the binding energy of the electron, respectively. The photoelectric effect dominates in human tissue at energies lower than 100 keV [36]. Since typically an electron from inner shells is ejected, characteristic x-ray or release of Auger electron should be expected after the photoelectric process.

Compton scattering

In this process which more likely occurs with $0.1 \sim 2$ MeV γ photons in human tissue [36], a loose electron in an outer orbital interacts with the incident γ photon, absorbs a small portion of its energy and flies out from the atom. Consequently, the γ photon is scattered with lower energy and further undergoes another interaction in the matter.

Pair production

In cases where the incident photon has higher energy than twice the rest-mass energy of an electron ($E_\gamma > 1.022$ MeV), there is a possibility that the photon interacts with the strong electric field of a nucleus in the matter and produces a pair of positron and electron. This possibility is narrow when the energy is just a few 100 keV higher than 1.022 MeV. Instead, for energies as high as several MeV, this phenomenon is more likely to happen.

The excess energy over 1.022 MeV is shared by the produced positron an electron as kinetic energy.

Coherent (Rayleigh) scattering

Coherent or Rayleigh scattering is a process in which a photon interacts with an atom as a whole. The photon is deflected in this process without any loss of energy. This process occurs in low energies ($\ll$ 50 keV) and should be considered in some cases where precise transmission of photons is measured such as X-ray computed tomography [49].

Attenuation of γ-ray in matter

γ-ray undergoes one or a combination of photoelectric effect, Compton scattering, and pair production processes and attenuates exponentially through its trajectory path.

$$I(x) = I_0 e^{-\mu_l.x} \tag{2.13}$$

Here, I is the intensity of the beam after traveling the distance x, and μ_l is the linear attenuation coefficient. For a specific absorber, the linear attenuation coefficient is given by:

$$\mu_l = \tau + \sigma + \kappa \ \ (\text{cm}^{-1}) \tag{2.14}$$

where τ, σ, and κ are the photoelectric, Compton, and pair production coefficients, respectively. μ_l is smaller for γ-rays with higher energies and is greater for materials with higher densities. In the case of 511 keV γ-rays, μ_l is ~ 0.1cm^{-1} in human tissue, and ~ 1cm^{-1} in scintillators [36].

2.4.   Applications of Gamma Rays in Medical Imaging

γ-rays are the highest energy electromagnetic waves arising from radioactive decay of an atom or as a subsequent result of the interaction of emitted particles such as neutron

or β$^+$ with the matter. In medical applications, typically low-energy γ-rays (100-511 keV) are used since while they can penetrate living tissue, they can be stopped and efficiently detected by using some materials in detector design [50]. There are more than 20,000 γ-ray-based medical imagers installed in hospitals worldwide [51]. In all gamma imaging modalities, a radioactive nuclide mounted on a biomolecule is introduced into the body. The biomolecule is biologically designed to be consumed by target cells. Thereby, localized accumulation of radioactivity in an organ gives information about the target cells. For instance, cancerous cell and tumors consume an excessive amount of glucose; hence fluorodeoxyglucose (^{18}FDG) which emits positron and subsequently γ-rays is injected into the body to be accumulated in the tumor area.

Several mechanisms for in vivo gamma imaging have been developed since the early 1950s [52] after the introduction of pinhole gamma camera by Copeland *et al*. in 1949 [53]. Hal Anger was first to report the application of pinhole gamma camera in medicine. Thereafter, this medical imaging was called Gamma Camera, Anger Camera, or Scintillation Camera. The imaging techniques underwent various advancements through time and SPECT and PET were introduced [54–56]. Recently, the utilization of double-photon emitting nuclides has drawn attention and some imaging techniques have been introduced [3, 4, 57]. In this chapter, major γ-ray-based medical imagers are briefly described with their pros and cons.

2.4.1. Gamma Camera

Early Gamma cameras were using a pinhole aperture in front of a scintillator crystal coupled to a photographic plate or film [52] as shown in Figure 2.1. The projection of γ-rays through the pinhole was recorded to form a planar image the same way as a photographic pinhole camera.
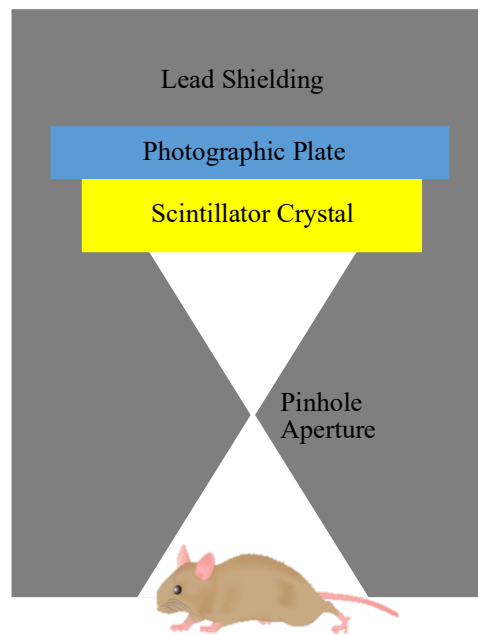
Figure 2.1. Schematic view of a pinhole Gamma Camera introduced by Hal Anger

All components have been substantially advanced through time to provide better images. First, Anger himself replaced the photographic plate with a photomultiplier tube assembly to enhance the image [58]. Next, coded aperture masks and parallel-hole collimators were introduced to increase the detection efficiency of the system. And later, the block crystal was replaced by an array of crystals separated by reflectors for better positioning of the detected γ photon [59, 60].

Several types of Gamma Cameras have been commercialized and used in hospitals. The most common types are single-headed and dual-headed gamma cameras [58]. In both types, the camera heads are flexible and can be positioned at any angle to take multiple images. A great advantage of dual (or multiple)-headed cameras is that two (or more in the cases of multiple-headed cameras) different planar images can be obtained at the same time. The spatial resolution of commercial Gamma Cameras with a large field of view

(FOV) is about 3 mm [61]. Small Gamma Cameras for specialty purposes or for animal studies have been developed with sub-mm spatial resolution [62].

One of the main drawbacks of Gamma Camera is its low sensitivity due to the presence of a collimator. In other words, the collimator rejects an inordinately large number of emitted photons. It also has a poor capability of background rejection and thereby an effective shielding is mandatory. Another disadvantage is planar imaging. One image does not give enough information about the tissue. The incident rays may have come from different depths in tissue yet projected on the same image. This issue is resolved in tomographic imaging using Gamma Camera, i.e. in Single-Photon Emission Computed Tomography (SPECT).

As discussed above, Gamma Camera has low sensitivity. Roughly speaking, only 1 per million of all photons can pass through the collimator [63]. Another technique, generally used in astrophysics, is Compton imaging in which no collimator is used. In Compton Camera, a scatterer and an absorber layer of detectors are utilized. Based on the detected energies in scatterer and absorber in case of one event, the original angle of the incident photon can be estimated with a cone. The intersection of all detected cones by using some reconstruction algorithms gives the final image. Compared to collimator-based imagers, Compton Camera has better sensitivity in the regime where Compton scattering is the dominating interaction process. Therefore; this technique is more popular in nuclear imaging with high-energy γ-rays and in astrophysics where Compton scattering dominates over photoelectric effect. In medical applications with low-energy γ-rays, this method is not so practical. There are few applications of Compton Camera in medicine, basically for on-line monitoring during proton/neutron therapy where high energy gamma rays are emitted as a subsequent process of heavy particle interaction with tissue [64].

2.4.2. Single-Photon Emission Computed Tomography

As discussed before, in Gamma Camera, the camera head can rotate around the patient to take images from different views. These images are projections of the 3D distribution of the radionuclide on a 2D image. In Gamma Camera, typically limited views (projections) are scanned. Tomography is an approach to combine these projections to give a better 3D intuition of the object. If many different angular projections are scanned, these projection data could be combined using some mathematical algorithms to present more precise information of the 3D object. Then, any slice of the object could be reconstructed from the dataset. This approach is called computed tomography. Single-photon emission computed tomography is a computed tomography approach in which a gamma camera rotates around the object and scans many projections. These projections are combined into a sinogram from which images of selected planes and slices are reconstructed by using some mathematical algorithms, namely filtered back-projection (FBP) or maximum-likelihood expectation-maximization (MLEM) [54, 65, 66].

A great advantage of SPECT over planar imaging of Gamma Camera is its significant contrast-to-noise ratio in the image. This is due to the fact that the image presented by Gamma Camera is a superposition of all adjacent slices, while SPECT can provide individual images for each slice. In other words, SPECT provides more accurate quantitative information of radioactivity at any depth or location within the organ [67].

Despite several advantages over Gamma Camera, SPECT still suffers from low sensitivity because of using a collimator as well as covering a limited solid angle for the detection of emitted γ photons. In addition, the rotation of the camera raises mechanical challenges in the system development. It also takes several minutes to rotate and acquire all projections, which makes it incapable of imaging fast biological processes. To

overcome these drawbacks stationary SPECT systems with multiple camera heads (modules) arranged in polygonal configurations have been developed [68]. This approach significantly increases the sensitivity, signal-to-noise ratio (SNR), and spatial resolution of SPECT, and enables real-time imaging since all projections are recorded simultaneously.

SPECT is frequently used for cardiac imaging, particularly in studies on myocardial perfusion for assessing coronary artery disease and heart muscle damage resulting from infarction, and for cerebral imaging of brain tumors, brain functions, cerebrovascular disease, seizure, and psychiatric disorders [69]. It is also applied in oncology to visualize primary or metastatic lesions in the thorax and abdomen, where planar imaging by Gamma Camera cannot localize the tumor in the depth of the organ precisely [69].

2.4.3. Positron Emission Tomography

Right after the discovery of the positron in the early 1930s, Klemperer showed that two 511-keV photons are emitted simultaneously in opposite directions following a positron emission [70]. However, it took two decades to utilize this unique characteristic of β^+-emitting radionuclides in nuclear medicine [71]. The first use of positron in nuclear medicine dates back to 1945 in a study where $[^{11}C]$-CO was used in a single-photon mode to observe the elimination of carbon monoxide from the body [55, 56, 72]. Later on, potential medical applications of positron-emitting radionuclides produced in a cyclotron were discussed by Mitchel [73]. Wrenn *et al*. [71] were the first to report coincidence detection of 511-keV photons emitted as a result of β^+-decay. Their detection system simply consisted of a pair of scintillation detectors facing each other and a source that was placed between them. Later in 1953, Brownell and Sweet designed a multi-detector system for coincidence detection of annihilation photons [55, 56, 74]. The idea of a

circular detector array, which is still in use in modern positron emission tomography, dates back to the early 1960s at Brookhaven National Laboratory (BNL) where a ring of 32 scintillation detectors was designed to scan a single layer of the human brain [75].

A great advantage of PET over SPECT is that due to the angular correlation (180°) between coincidence photons, there is no need to use collimators. This tremendously increases the sensitivity even though unpaired photons are skipped during data processing. Skipping unpaired photons provides an intrinsic background rejection which results in higher SNR and CNR than SPECT. Another advantage is that spatial resolution is limited by the detector pitch which can be narrowed down to 0.5mm for 0.25-mm spatial resolution [8, 9]. On the contrary in SPECT, spatial resolution is limited by collimator resolution, and reducing the hole size substantially decreases the sensitivity of the system.

Another innovation in PET within its historical advancement was the idea of extracting the difference in time-of-flight (TOF) of annihilation photons [76]. This idea gained more attention after emerging of fast scintillators in the 1980s and early versions of TOF-PET scanners were developed [76, 77]. Advancement in detector design hitherto has continuously moved the research and instrumentation of PET and TOF-PET scanners forward.

One major issue in PET is its non-uniform spatial resolution over its FOV. Spatial resolution is best in the center of FOV, and it degrades radially. This is called parallax error which arises from the length of crystal that should be long enough to efficiently stop 511-keV photons. Several methods have been introduced to identify the depth of interaction (DOI) of incident γ photon in the crystal in order to remove or reduce parallax error. This will be discussed in detail in Chapter 5.

Positron emission tomography has been extensively used in nuclear medicine to study

various biological functions since 1953 when Brownell and Sweet used their multi-detector coincidence system to localize brain tumors [55]. In another report, Ter-Pogossian at Washington University of St. Louis used ^{15}O to measure regional metabolism in tumor-bearing rats [55, 56]. In the 1960s, the circular scanner developed at BNL was used to measure regional cerebral blood flow [55, 56, 74]. That period, gaseous positron-emitting tracers were widely used to study lung functions including ventilation, perfusion, and gas exchange [78]. In the late 1960s, Ter-Pogassian and his colleagues measured regional tissue oxygen consumption by injecting $[^{15}O]$-H_2O directly to the carotid artery [55].

The milestone in the history of PET was its commercialization in the 1970s [78] followed by the release of commercial PET scanners by two brand companies, General Electric and Computer Technology Imagery, in the early 1980s that expanded applications of PET from research to clinical studies [76]. They were initially used to measure perfusion, oxygen use, and glucose metabolism in brain tumors [78]. In 1982, Di Chiro *et al*. reported the use of ^{18}F-FDG to study cerebral gliomas, a type of brain cancer [78, 79]. They found a correlation between the rate of glycolysis and malignancy in primary cerebral tumors [79]. Meanwhile, ^{18}FDG was also used for high-contrast imaging of lung tumors [78] as well as imaging breast cancer [55]. Since then, ^{18}FDG has been used widely for the diagnosis of tumors, disease management, and treatment monitoring [78]. During the last three decades, PET has found a great number of clinical applications. It was applied to study Parkinson's and Alzheimer's diseases first in the 1990s [55]. It is interesting to mention that PET has been also used in some researches on addiction, schizophrenia, and HIV infection [55].

3.   FUNDAMENTALS OF POSITRON EMISSION TOMOGRAPHY

In the previous chapter a brief description and history of positron emission tomography (PET) as one of the gamma imaging modalities being used in healthcare as well as in clinical and biological studies were provided. Advantages of PET over Gamma Camera and SPECT as well as some challenges and issues were also addressed. In this chapter, a more detailed overview of the principle, components, and methodologies of PET imaging is presented. First, the basic principle of PET imaging is given in the first section. Common radiotracers and radiopharmaceuticals used in PET imaging are also described with their applications in this section. In section 3.2, radiation detectors used in PET systems are presented including scintillator crystals and photodetectors, and the detection efficiency and sensitivity of the system are explained. The data processing and image reconstruction algorithms are briefly described in section 3.3.

3.1.   Principle of PET Imaging

In PET, a positron-emitting radiopharmaceutical, which is an active biomolecule labeled with a β^+-emitter radionuclide, is inserted into the body. The biomolecule is biologically designed to be absorbed by the target cells. Only a few positron-emitting

radionuclides are suitable for clinical studies, which are mainly produced in a medical cyclotron. ^{18}F, ^{11}C, ^{13}N, and ^{15}O are the main radionuclides produced for PET imaging. These nuclides merely emit positron; thus, they are suitable for PET [81].

^{18}F is the most common radiotracer for PET. It is used in various pharmaceuticals such as fluorodeoxyglucose (FDG) compound. ^{18}F has a 110-minute half-life and hence it is merely used in the hospitals and institutes where a medical cyclotron is locally accessible. FDG is primarily used for the study of metabolism in tissue, mainly brain and heart, and for the detection of various tumors. Sodium fluoride-[^{18}F], usually used for the synthesis of FDG and other radiopharmaceuticals, itself can be used for bone scintigraphy [82]. [^{18}F]-fluorothymidine (FLT) is another pharmaceutical labeled with ^{18}F, which is used in DNA-based studies and characterization of tumors in humans [82]. Another ^{18}F-labeled pharmaceutical is fluoromisonidazole (FMISO) used in PET for the detection of hypoxic tissues [82].

The ^{11}C produced in cyclotrons has a short half-life of ~ 20 minutes and thus it must be produced in a local cyclotron. Some ^{11}C-labeled pharmaceuticals are sodium acetate-[^{11}C] typically used for the measurement of oxygen consumption in the heart, [^{11}C]-flumazenil for the characterization of the neuroreceptors in neurons, [^{11}C]-methylspiperone for the study of neurological disorders, [^{11}C]-raclopride for the detection of various neurological and psychiatric disorders such as Parkinson's disease and schizophrenia, and [^{11}C]-choline for the detection of various tumors [82].

The ^{13}N is also produced in a local cyclotron and it has a 10-minute half-life. It is commonly provided as ^{13}NH$_3$ to measure myocardial and cerebral perfusion [82]. The ^{15}O has a very short half-life of just 2 minutes and is also produced in a medical cyclotron which is locally available. H$_2$^{15}O (positron-emitting water) is used for myocardial and

cerebral perfusion studies [82].

Some other radionuclides are produced through radionuclide generators consisting of the parent and the daughter nuclides in an apparatus which makes it possible to separate the daughter nuclide from the parent nuclide [83]. ^{62}Cu and ^{82}Rb are examples that are used to label some PET pharmaceuticals for measuring myocardial perfusion [82].

Once a positron is emitted from one of the aforementioned radiopharmaceuticals, it is deflected many times by electrons in the tissue so that its kinetic energy abates. Once the positron is at rest (typically in a very short range), eventually it combines with an electron, and then both are annihilated. In some cases, the combination of positron and electron produces a metastable species called positronium with an average half-life of 10^{-7} seconds [36] after which the two particles are annihilated. However, in the water and human tissue, the direct annihilation is more likely to happen. Following the annihilation of positron and electron, a pair of 511-keV photons are emitted in opposite directions.
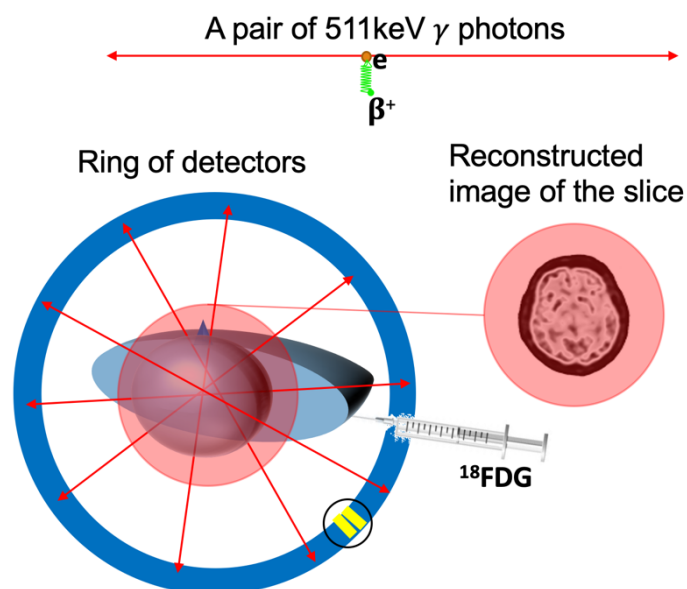
Figure 3.1. Basic concept of positron emission tomography.

As schematically shown in Figure 3.1, a PET scanner typically consists of a ring of detectors to detect the pairs of annihilation photons through coincidence detection. Each coincidence makes a line of response (LOR) connecting the pair of detectors that were involved in the coincidence detection. The LORs are registered into a sinogram which is further processed through an image reconstruction algorithm to give the final image.

3.2.   PET Detectors

The detection of γ photons requires an optical circuit connected to an electronic circuit. The optical circuit converts the high-energy photon to a number of light photons that can trigger a photosensor and initiate an electronic signal. The electronic circuit transfers and records the signal which can be further analyzed using a processing chip or a computer. In this chapter, the components of the detection systems used in γ-ray imaging are discussed. The optical circuit typically consists of a scintillator crystal and a photodetector. The combination of these two components is the so-called scintillation detector shown in Figure 3.2. There are other types of radiation detectors, namely the proportional gas chambers and semiconductor detectors. However, they both have poor detection efficiency in comparison with the scintillation detectors [36]. The electronic circuit typically includes an RC circuit to amplify and transfer the signal to an ADC circuit to digitize and record the signal for processing.
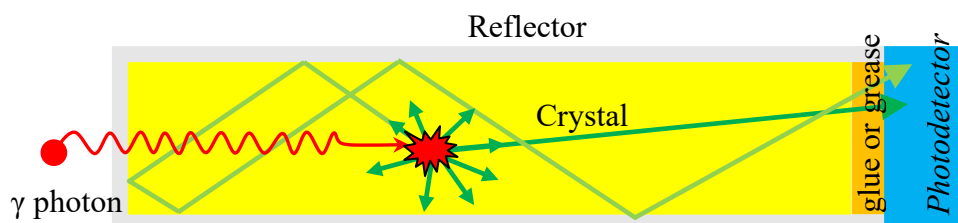
Figure 3.2. The general concept of scintillation detectors

3.2.1. Scintillators

Scintillator crystals are the main components for γ-ray detection as they not only stop high-energy photons but also illuminate light photons upon the interaction of γ photons in their media. The phenomenon is called scintillation. In this process, the incident γ photon interacts with a high-density medium and causes ionization or excitation of atoms or molecules on its track. The ionized or excited atoms/molecules subsequently recombine or deexcite and release the energy. This energy typically turns into the molecular vibrations in gases and liquids, and into the lattice vibrations in crystals; however, in some materials, this energy initiates a photoluminescence process [84]. These materials are called scintillators and have been widely used in radiation detection. There are two types of scintillators; organic substances dissolved in liquid solutions or in the form of plastic or crystals, and inorganic scintillators in the form of solid crystals [84, 85]. The ideal scintillator should efficiently convert the kinetic energy of γ photons into detectable light with a linear conversion response over a wide range of energies and a short decay time to generate a fast signal pulse. Meanwhile, it must be transparent or at least have a long absorption length over its own emission spectrum, and it must have a refractive index near that of glass for optimum optical coupling to photodetectors. Nonetheless, no material can perfectly meet all these requirements; therefore, the choice of crystal always depends on the system requirements and purposes [85]. For instance, in nuclear imaging for decommissioning or in astrophysics; high energy-resolution detectors are needed to discriminate the sources of radiation and thus scintillators with high yield are preferred. On the other hand, in TOF-PET for instance, a fast response is quite essential and hence scintillators with fast rise time and a relatively short decay constant are needed.

Organic scintillators

The scintillation process in organic materials stems from transitions in the energy level structure of a single molecule in any physical state. This means there is no necessity to crystalize the material for scintillation. Consequently, organic scintillators are produced in three physical forms; pure organic crystals, liquid organic solutions, and plastic scintillators. The organic molecules used in these scintillators mostly have certain symmetry properties in their electronic structure known as π-electron structure. In these molecules, the energy spacing between ground state (S_0) and first singlet excited state (S_1) is 3~4 eV whereas the differences between higher singlet states are smaller [85]. The scintillation process is initiated by absorbing the kinetic energy of the incident γ photon that excites the electronic configuration. The higher singlet electronic states usually transit to S_1 state through internal conversion. Consequently, a population of molecules after a negligibly short time are in their S_1 state, which prompts the photoluminescence process through transition into any vibrational state of the ground electronic state (S_0). This prompt fluorescence typically has a decay constant in the order of few nanoseconds which produces a fast signal desirable for radiation detection. There are other possible deexcitation modes for these molecules in which the excitation energy ends up in thermal heat without initiating any photoluminescence. All these modes are termed *quenching*. Generally, the existence of impurities in these materials results in excess quenching mechanisms. Thereby, in the fabrication process of organic scintillators, manufacturers try to avoid or remove impurities from the material in order to provide high scintillation efficiency. However, only two pure organic crystals have achieved widespread popularity in radiation detection. Despite having the highest scintillation efficiency and greatest light yield among all organic crystals, they are hard to manufacture and difficult to work with

since they are quite fragile and, more importantly, their scintillation efficiency depends on the angle of the incident γ photon [85]. Liquid solutions, on the other hand, have less efficiency but they are more cost-effective; particularly in certain applications where large volume detectors are required, liquid organic scintillators are the only practical choice [85]. Plastic scintillators are the equivalent solid solutions of liquid solutions, which are mechanically stable and can be easily manufactured in a variety of forms even as ultrathin films with thickness as small as 10 μm. They have relatively short decay time and high light yield and thereby they are a good choice for coincidence detection when timing resolution is of importance; i.e. in TOF-PET. However, they are quite vulnerable if they come in contact with organic solvents. In addition, they are prone to radiation damage and their scintillation efficiency degrades under doses in the range of $10^3 \sim 10^4$ Gy [85].

Inorganic scintillators

The scintillation mechanism of inorganic scintillators is completely different from that of organic materials. This mechanism can be observed merely in the crystalline form of material. In a pure inorganic crystal, electrons can be either in the valance band of energy – that are the electrons bound at the lattice site of crystal – or in the conducting band, which are the free electrons that can migrate throughout the crystal. The gap between the conducting band and valence band is called the forbidden band since electrons can never be found in that range of energy. Therefore, upon the excitation by ionizing radiation, an electron from the valance band moves to the conducting band and leaves a hole in the valance band. Because the gap (the forbidden band) is typically large, the return of the electron to its valance band by emitting a photon is quite unlikely, and even if it occurs, the resulting photon has higher energy than visible light to be detected by photodetectors. To overcome this effect, a certain amount of impurity, called an activator, is added which

has a ground state and excited states within the forbidden band of crystal as shown in Figure 3.3. This provides intermediary bands, termed luminescence centers or recombination centers [85], through which the excited electron can transit to the valance band by emitting a low energy photon in the range of visible light that can be easily detected by a photodetector. Because of the energy band structure of the crystal, the illuminated photons are less likely to be absorbed by the crystal itself, and they can propagate a relatively long track to hit the photodetector. The decay time of scintillation is limited by the lifetime of the activator's excited states which is usually in the range of 30-500 ns. This is one disadvantage in comparison with organic scintillators. However, due to their higher atomic mass and density, inorganic scintillators have higher stopping power against high-energy γ photons and consequently better detection efficiency than organic scintillators. In addition, inorganic scintillators typically have higher light yield and more linear energy response than organic scintillators due to much lesser quenching processes [85].

In PET, mostly inorganic scintillators are being used because of their high density and high effective atomic number to stop the 0.511-MeV γ photon. Inorganic scintillators are, in fact, the indispensable components of positron emission tomography, which have been used from the early days of coincidence detection with positron-emitting nuclides. Wrenn *et al.* [71] used a pair of thallium-doped sodium iodide (NaI:Tl) crystals coupled individually to photomultiplier tubes. Other scintillation crystals were developed including $CdWO_4$, CsI:Tl, CsF, CsI, LiI:Eu, and cerium-doped silicate glass [86]. In the 1970s, bismuth germanate ($Bi_4Ge_3O_{12}$ or BGO) with a high detection efficiency attracted many researchers in the field [76, 87, 88]. Upon the emergence of BGO, fabricating pixelated crystals gained currency since the mid-1980s [88, 89]. It was later shown that

PET systems with block crystals have a slightly worse spatial resolution than systems with pixelated crystals [5–7]. In the early 1980s, the fast (600 ps) BaF_2 scintillator found its application in TOF-PET [76]. Even though BaF_2 scintillators had fast decay time, soon they were abandoned due to their low sensitivity and low light yield [76]. Instead, cerium-doped lutetium orthosilicate (Lu_2SiO_5:Ce or simply LSO) crystals with high sensitivity, high light yield, and a relatively short decay time of 40 ns [76, 88, 90] began to prevail in the detector design to this day. $LaBr_3$:Ce [91] with 16 ns decay time [76] and also LYSO [92] are more recent crystals which are being used in the past two decades. Common scintillator crystals used in PET detectors are listed and compared in Table 3.1 with reference to [36, 84, 85, 93–105].

In recent years, Ce:GAGG (cerium-doped $Gd_3Al_2Ga_3O_{12}$) [106] has gained currency in the field due to its outstanding scintillation properties. The relatively high density and effective atomic number (Z_{eff}) of GAGG provide enough power to stop the 511-keV photon. Its light yield (57,000 photon/MeV) facilitates the detection system with a high energy resolution [94]. Another advantage of GAGG crystal is that it is not self-radiative. Scintillators which are made of lutetium (LSO, LYSO, LuAG, and LuAP) are self-radiative due to the radioactivity of lutetium.
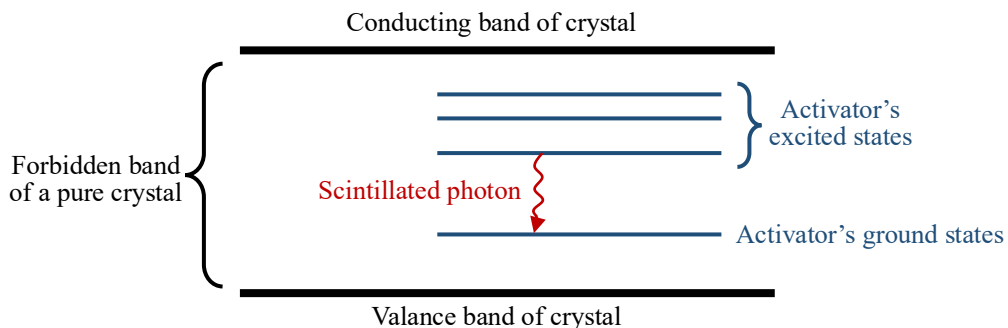
Figure 3.3. Energy band structure of a crystal with inserted impurity (activator)

Table 3.1. Properties of common scintillators used in PET

Crystals / Properties	NaI:Tl	CsI:Tl	BaF$_2$ (fast)	BGO (Bi$_4$Ge$_3$O$_{12}$)	GSO:Ce (Gd$_2$SiO$_5$)	LSO:Ce (Lu$_2$SiO$_5$)	YSO:Ce (Y$_2$SiO$_5$)	LYSO:Ce (Lu$_x$Y$_{2-x}$SiO5)	YAG:Ce (Y$_3$Al$_5$O$_{12}$)	YAP:Ce (YAlO$_3$)	LuAG:Ce (Lu$_3$Al$_5$O$_{12}$)	LuAP:Ce (LuAlO$_3$)	GAGG:Ce (Gd$_3$Al$_2$Ga$_3$O$_{12}$)	LaBr$_3$:Ce
Density (g/cm^3)	3.67	4.51	4.89	7.13	6.71	7.4	4.53	7.3	3.67	5.37	6.73	8.34	6.63	5.29
Z$_{eff}$	50.6	54	52.2	74.2	58.6	65.5	34.2	65	32	32	59	65	54.4	46.9
Decay time (ns)	230	1000	0.6	300	60	40	70	50	70	25	70	18	88	16
Attenuation length (cm) of 511 keV	2.88	2.07	2.2	1.05	1.43	1.16	2.58	1.16	3.5	2.7	1.3	1.05	1.59	2.13
Light yield (photon/keV)	38	52	2	6	10	29	46	25	35	25	25	12	57	63
Wavelength of peak emission (nm)	410	540	220	480	440	420	420	428	550	370	535	365	520	358
Index of refraction	1.85	1.8	1.56	2.15	1.91	1.82	1.8	1.82	1.82	1.95	1.84	1.97	1.87	1.88
Energy resolution (FWHM % @ 511 keV)	6.6	4.53	11.4	10.2	9.5	10.1	12.5	20	7	10.8	6.7	15.5	7.1	2.9
Hygroscopicity	Yes	Slightly	No	No	No	No	No	No	No	No	No	No	No	Yes

3.2.2. Photodetectors

After the light is illuminated through the scintillation process, a photodetector is needed to convert visible light into an electric signal. The photodetector could be a photomultiplier tube (PMT), an avalanche photodiode (APD), or a silicon photomultiplier (SiPM) pixel.

Photomultiplier tube (PMT)

A PMT is a vacuum tube with a photocathode at the entrance and an anode at the end and a number of dynodes to multiply emitted electrons as shown in Figure 3.4. The photocathode is usually a cesium antimony alloy (CsSb) [84, 93] that absorbs light photons and emits photoelectrons with a quantum efficiency of 20~30% [107]. A high voltage is applied between the photocathode and anode, which is equally incremented between the dynodes. Once a photoelectron is released from the photocathode, due to the strong electric field between the photocathode and the first dynode, it is accelerated toward the dynode. The dynodes are coated with a material that has a relatively high secondary emission characteristic (high multiplication factor δ), such as BeO, MgO, or Cs_3Sb [107]. The photoelectron hits the first dynode and makes it release δ electrons which hit the next dynode and make it emit more electrons. This multiplication continues to the last dynode and a large number of electrons (e.g. δ^{10} electrons in the case of 10 dynodes) flow into the anode and an electric signal appears at the output. PMTs are quite large and expensive, but they can provide a fast and strong output pulse [93].

Avalanche photodiode (APD)

Photodiodes are light-sensitive semiconductors such as silicon which are ionized when they are irradiated by visible light. As a result, a number of electrons are released, which they gain enough energy through acceleration in presence of a high voltage (in range of

20~30 V) and further ionize the semiconductor. The newly released electrons enter the same process as well and make the semiconductor produce an avalanche of charge. Because of this avalanche process, these photodiodes are termed as avalanche photodiodes. This process triggers an electric current flow through the external circuit, which as a consequence, generates an electronic signal. The high internal gain of APDs offers a very good sensitivity, high signal to electronic noise ratio, and high energy resolution. In addition, their compact design and relatively high counting efficiency (and thus better energy resolution) have made APDs quite advantageous over PMTs.

Silicon photomultiplier (SiPM)

When the high voltage applied to a semiconductor photodiode exceeds the breakdown voltage of the device (typically around 30 V), a single self-sustaining avalanche is formed by merging all the multiplication regions in the semiconductor. This is the Geiger mode of the photodiode, in which even a single charge can be multiplied with no limit. Thereby, such photodiodes are highly sensitive and can detect even a single photon, for which they are called single-photon avalanche photodiodes (SPADs). The produced charge will be depleted by an RC circuit, and an electric pulse is generated.
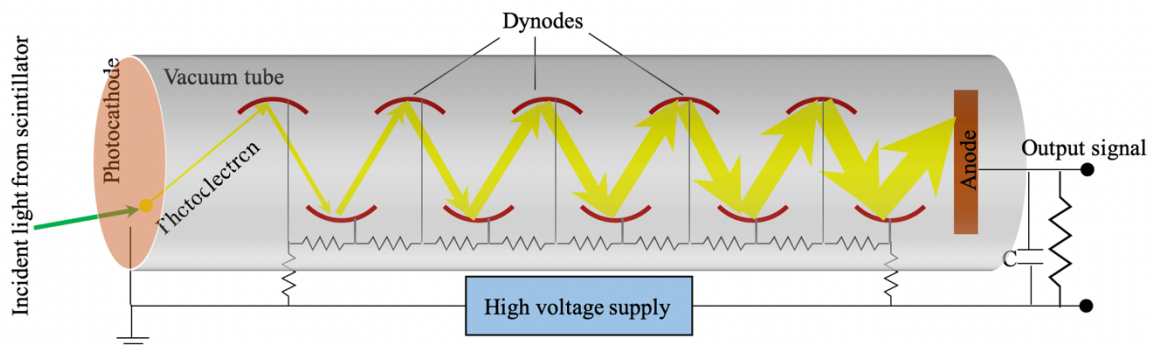

Figure 3.4. Schematic view of a photomultiplier tube

Even though SPADs are sensitive even to a single photon, they cannot provide any information on how many photons have hit them when a pulse is shaped. In other words, disregarding the number of photons entering the photodiode, just a single charge may suffice it to start the Geiger-mode avalanche. Therefore, an array of thousands of microscopic Geiger-mode photodiodes has been developed so that there would be a little chance that a microscopic photodiode is hit by a scintillation photon while it is in operation for previous incident scintillation photon. Such array is called silicon photomultiplier (SiPM), solid state photomultiplier (SSPM), or multipixel photon counter (MPPC) as it counts the incident photons. The number of microscopic photodiodes should be as large as a multiple of the number of scintillation photons expected to hit the SiPM.

In addition to their high sensitivity and compact design, SiPMs have relatively high counting efficiency as well as relatively good timing resolution of a few hundred picoseconds. Since SiPMs are insensitive to the strong magnetic fields, they are the appropriate choice for hybrid PET/MRI scanners.

3.3.   Data Processing and Image Reconstruction

The PET detection system is designed to detect the pairs of annihilation photons propagating in opposite directions without being scattered. The detection of such a coincidence is a true event. Each pair should be detected within a predefined time window, typically up to 15 ns depending on the system timing limitations. Detectors must be calibrated for energy resolution so that only events in the calibrated range for the 511-keV photopeak are selected. The coincidence detections passing through the aforementioned conditions are called prompts [110, 111]. However, prompts are not always representing true events. A prompt could be a random coincidence of uncorrelated

annihilations or a coincidence of scattered photons. A random coincidence arises when two annihilations occur almost simultaneously and from each pair, one photon is detected and the other is missed. Consequently, the two photons which are detected as a coincidence are not representing a true annihilation. The coincidence detection of scattered photons is also very common in PET scanners with poor energy resolution. Multiple coincidences are also possible when three or more photons are detected within a time window, but these events can be discarded easily in the processing unit. There is also a narrow possibility (less than 1%) that three photons are emitted in 120° directions with respect to each other [36]. However, it is preferred to discard such a case since the possibility of detecting three uncorrelated photons is higher.

In order to reduce the random and multiple coincidences, the detector ring is usually shielded by lead layers at both sides [109]. Individual detectors are connected through a coincidence measurement circuit only to detectors within a portion of the ring on the opposite side to merely cover the object area (see Figure 3.5). In modern systems, there is no physical circuit for this; instead, this task together with the energy and time window setting is accomplished by the processing unit. Once a prompt is extracted, a line of response (LOR) connecting the two corresponding detectors is saved in terms of polar coordinates (r,φ) using positioning information of the detectors, where r is the distance of LOR from the center of the ring, and φ is the orientation angle of LOR (the angle between r and X-axis). This is shown in Figure 3.6. The LOR coordinates are stored in a sinogram with the horizontal axis representing r and the vertical axis representing φ [110, 111]. Each pixel in the sinogram corresponds to a specific LOR. Once an LOR is saved after a coincidence detection, a count is added to the corresponding pixel in the sinogram.
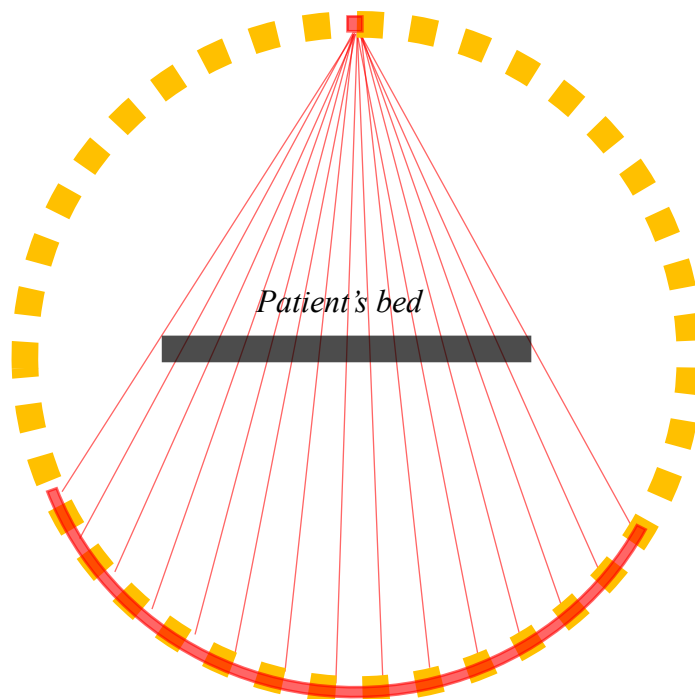
Figure 3.5. Coverage angle of individual detectors. For the selected detector, only coincidence events with highlighted detectors are accepted.
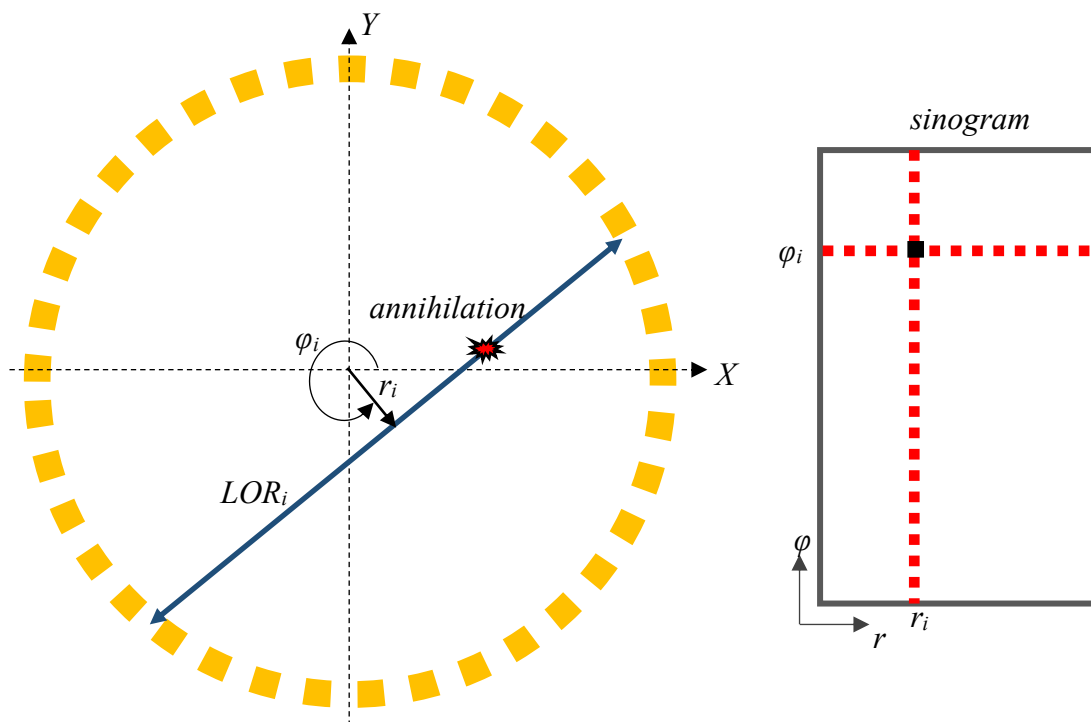

Figure 3.6. Storing coincidence data into a sinogram. The black pixel in the sinogram corresponds to LOR_i with (r_i, φ_i) coordinates.

A sinogram is recorded for each slice being scanned. Next, data correction filters, such as sensitivity correction, arc correction, etc. are applied to each sinogram to improve the quality of final images. The advantage of making a sinogram is that the coincidence data (LORs) are kept and correction can be simply applied by giving specific weights to them. After these preparations, the image is reconstructed by applying either an analytical or iterative method. The sinogram is in fact the *X-ray* transform of the image, which is the same as Radon transform in 2D [112]. Therefore, the exact analytical reconstruction is solving the inverse Radon transform to transform back the data from the sinogram space (r, φ) to the image space (x, y). This can be done by applying the Fourier transform to the sinogram function with respect to r. Subsequently, the sinogram is transformed into the Fourier space (v, φ). The sinogram in the Fourier space is given by [112]:

$$S(v, \varphi) = F(v_x = v \cos \varphi \, , v_y = v \sin \varphi) \qquad (3.5)$$

$F(v_x, v_y)$ is the Fourier transform of the image $f(x, y)$. By solving the inverse Fourier transform, the image is reconstructed. These are the continuous expressions of functions. In practice, the discrete Fourier and inverse Fourier transforms are applied since the data is discrete. This method is called direct Fourier reconstruction and can be done by the fast Fourier transform (FFT) algorithm [112]. An equivalent to the direct Fourier reconstruction is the filtered-back-projection (FBP) algorithm [113, 114] in which the sinogram is first filtered by a ramp filter and then back-projected to the image space [112]:

$$S^F(v, \varphi) = |v| S(v, \varphi) \qquad (3.6)$$

$$s^F(r, \varphi) = \mathcal{F}^{-1}\{S^F(v, \varphi)\} \qquad (3.7)$$

$$r = x \cos \varphi + y \sin \varphi \qquad (3.8)$$

$$f(x,y) = \int_0^\pi s^F(x,y,\varphi)d\varphi \qquad\qquad (3.9)$$

The whole process can be discretized and applied to the recorded sinogram. Image reconstruction can also be done through iterative algorithms. Two major iterative algorithms are maximum-likelihood expectation-maximization (MLEM) [65] and ordered-subset expectation-maximization (OSEM) [66]. An advantage of these iterative algorithms over the FBP is that the physical properties of the system as well as the physical laws of radiation interactions with the matter can be modeled more precisely, while in FBP, a highly simplified model is used for the data analysis. Therefore, the impact of image reconstruction on the spatial resolution in the case of iterative methods is negligible. On the other hand, these methods are highly computational and consume a tremendous amount of memory and time.

4. DEVELOPMENT OF DIGITAL ANIMAL PET WITH 1-MM SPATIAL RESOLUTION

In this chapter, the design and components of the digital animal PET with 1-mm spatial resolution developed as a part of this research to evaluate the performance of the digital readout scheme are presented with results and discussion including challenges in the system development and calibration. This spatial resolution was chosen to compare the results with the state-of-the-art prototypes that have a 2-mm detector pitch. This is explained in section 4.1 along with the influence of individual coupling and readout in the spatial resolution of the PET scanner. Electronic readout in conventional PET is described in section 4.2 and the problems are addressed. In section 4.3, the concept of time-over-threshold method is explained, and several ToT methods are provided. In section 4.4, materials and methods to assemble the scanner are presented, the proposed digital readout scheme is described, and the experimental setup is explained. Results of experiments along with the discussions are presented at the end in section 4.5.

4.1. Spatial Resolution in PET

As a rule of thumb, the spatial resolution of a PET scanner in the center of the ring could be at best as small as half detector pitch. In 1993, Derenzo *et al*. [5] formulated the

spatial resolution based on studies on 20 different PET scanners to include several factors affecting the spatial resolution of a given PET system [6, 7]. Consequently, the full-width half-maximum (FWHM) spatial resolution in the center of a PET system with detector pitch d and ring diameter D can be calculated as follows:

$$\Gamma = a\sqrt{\left(\frac{d}{2}\right)^2 + (0.0022D)^2 + r^2 + b^2} \tag{4.1}$$

where a is the impact of reconstruction algorithm, b the impact of 2D positioning of the incident photon within the detector array, and r the positron range.

The impact of image reconstruction, a, is typically in the range of 1~1.3. It can be close to 1 in the case of applying iterative methods such as MLEM or OSEM and precise modeling of the system [66]. In the case of FBP reconstruction, this value is around 1.2 and slightly affects the spatial resolution of the system [6].

The impact of ring diameter in the $0.0022D$ term arises from $0.25°$ uncertainty in the $180°$ angular correlation of the annihilation photons. In fact, the annihilation photons do not propagate exactly in opposite directions. The $0.0022D$ factor is calculated from $0.5\tan(0.25°)D$ [6].
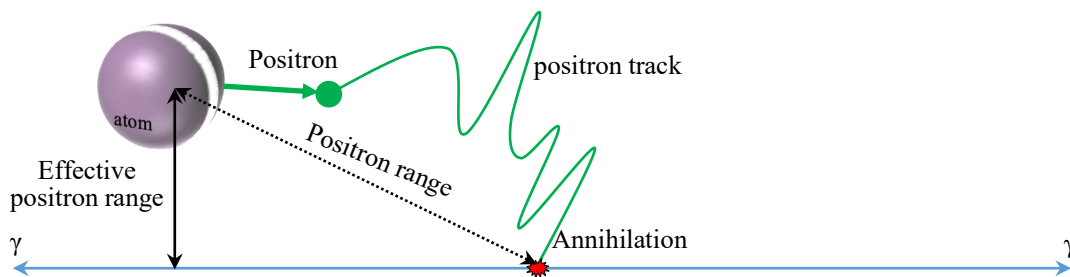

Figure 4.1. Positron track, positron range, and effective positron range

As shown in Figure 4.1, since positron is of a light mass it is deflected many times upon hitting a number of electrons and/or particles on its track. Thereby, it typically makes a zigzag track. Positron range is defined as the finite distance from the origin of the β^+-decaying nucleus to the position where the positron settled at rest and combined with an electron. This makes an uncertainty in localizing the β^+-emitting radiopharmaceutical. Due to the zigzag track, the positron range is relatively short (maximum 200-300 µm in tissue) However, the actual uncertainty is even smaller. Since the detection system relies on coincidence detection, the actual uncertainty coming from the effective positron range which is the distance from the origin of emitted positron to the LOR of the coincidence detection. The positron range in tissue was calculated in some studies [115, 116], and it depends on the energy of the emitted positron, which has a dependency on the radionuclide and the density of the medium.

4.1.1. Impact of Readout on Spatial Resolution

In equation (4.1), the last parameter, *b*, stems from the choice of detector design and readout system. Lecomte surveyed over a number of existing PET systems and summarized their spatial resolution [6]. According to his survey only systems with pixelated crystals and individual coupling can achieve spatial resolution as fine as half crystal pitch (*b* = 0). This is due to the fact that in such systems 2D positioning of the incident photon in the module is associated with a negligible error since detectors are almost isolated from each other. In the case of electronic encoding (resistive network with pixelated crystals) *b* is about 1.1 mm, and for systems with block monolithic crystals coupled to PMT arrays (light sharing method) *b* is about 2.1 mm. It should be noted that this parameter would completely dominate over the term $\frac{d}{2}$ (theoretical resolution) in

high-resolution PET systems where detector pitch is relatively small. Therefore, the demand for individual readout scheme for pixelated crystals become of great importance in such systems. By the same token, part of this presented work was devoted to developing and evaluating an effective readout scheme to provide individual coupling and readout for an animal PET with a 2-mm detector pitch.

4.2.   Electronic Readout in Conventional PET

In general, radiation detectors, and more specifically radiation counters, operate in the "pulse mode" which means they generate pulses of electrical current that are counted to determine the number of radiated photons/particles detected [117]. However, these pulses could be further analyzed for energy resolution as well as timing resolution in the case of coincidence detection. In brief, as schematically shown in Figure 4.2, the electronic readout for all types of detectors, ranging from simple counters to complex imaging modules, consists of an amplification circuit and a processing block. The amplification part could be a simple RC circuit depicted in Figure 4.3 for a simple SiPM readout, and the processing part could be a simple counter or a digitizer for further processing.

One important consideration in the amplification & shaping circuit is the input and output impedance of the circuit to have the optimum transfer of energy. The input impedance must match the output impedance of the photodetector, and the output impedance of the circuit must match the input impedance of the processing block. The capacitor in the circuit filters the noise and fluctuations associated with the photodetector output and shapes the signal, which facilitates the digitizing process of the pulse height analyzer (PHA).
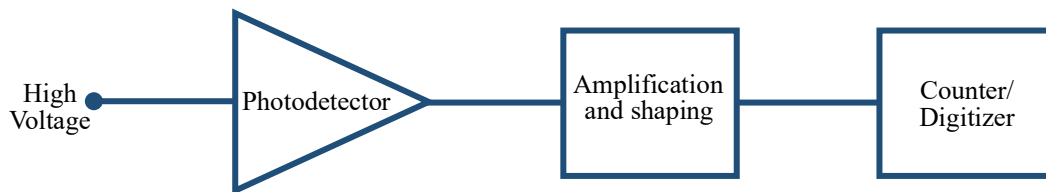
Figure 4.2. Schematic depiction of electronic components for radiation detection readout.
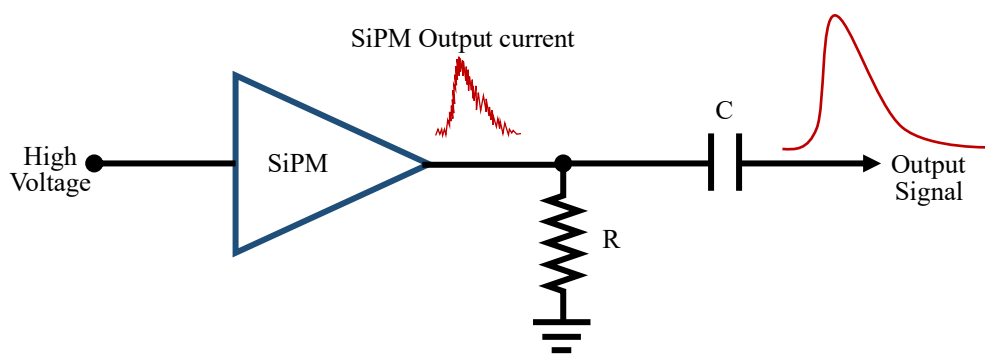

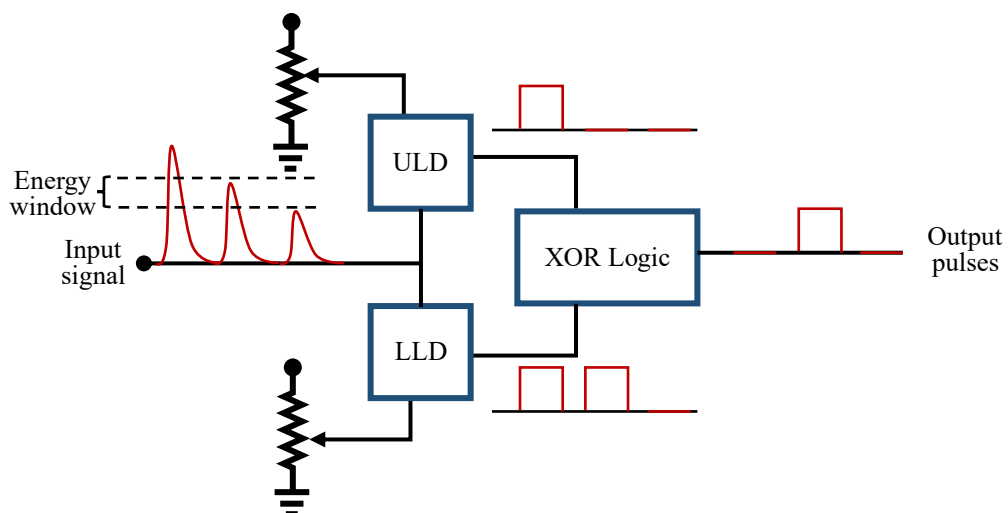Figure 4.3. Simple amplification and shaping scheme for a cathode type SiPM.

Figure 4.4. Block diagram of a single-channel pulse-height analyzer with sample signals and their corresponding output pulses from LLD, ULD, and final logic circuit.

4.2.1. Pulse-height analyzer

A PHA is a device used for energy-sensitive detectors to sort out detected photons of different energies and record a particular range of energy or skip scattered events and background activity [93, 117]. A PHA that does this process for only one channel at a time is called single channel analyzer (SCA) which has three major components; a lower-level discriminator (LLD) which passes the signals with energies higher than a defined threshold level, an upper-level discriminator (ULD) which passes signals with energies higher than the desired energy window, and a logic circuit which gives an output pulse when the LLD output is high but the ULD is low. The output pulses are of the same amplitude and duration, which no longer have the energy information – except that their energy is in the range of the predefined energy window. The block diagram of a single-channel pulse-height analyzer (SCPHA) is illustrated in Figure 4.4 [117].

4.2.2. Multichannel analyzer

The SCA is not a practical choice in imaging machines where a large number of channels receive signals individually. In such cases, multiplexing the detector outputs into one SCA is not a good idea since different detector channels have slightly different energy responses, and thus setting a universal energy window for all channels degrades the energy resolution of the system. On the other hand, employing a large number of SCAs costs a lot and requires tremendous effort to adjust the energy window separately for all the channels. This is where ADC steps in to provide us with a better PHA scheme; a multichannel analyzer (MCA). In an MCA, the ADC divides the pulse amplitude range into a finite number of intervals and sorts the incoming signals according to their amplitudes into those intervals. Conventional ADC records the signal as a 12-bit digital signal that means 4096 intervals for the pulse height range. In this way, all pulses are

recorded with their amplitudes that can be demonstrated on a histogram as a pulse-height

spectrum and then converted to an energy spectrum after calibrating with various sources.

Modern MCA boards are capable of analyzing data from several input ports (detectors)

simultaneously. Moreover, since the event selection based on energy can be carried out

after MCA, multiplexing the detector channels is plausible.

4.2.3. Multiplexing scheme for detector arrays

In systems with a large number of photodetector channels, individual readout costs a

lot and requires a tremendous number of cables, ports, and data acquisition units.

Therefore, multiplexing the channels into a smaller number of channels is quite essential.

The conventional method for multiplexing is connecting all channels through a resistive

network [15–19, 118, 119]. This concept originates from Anger's scintillation camera

[120] in which he connected all the PMT outputs through a resistor network with 4 output

signals and offered a method for better positioning of the detected photons. Thereby, it is

often called Anger Logic. In fact, in applications where a monolithic block crystal is

coupled to a PMT array – as in the case of Anger's camera – since the scintillated light is

shared among a number of neighboring channels, this method is effectively helpful for

2D positioning of the interaction point inside the crystal. Nonetheless, in systems with

pixelated crystals, it is used merely to reduce the number of channels. Despite several

advancements in the demultiplexing methods and algorithms, the positioning of the

original signal is always associated with some distortion which is more crucial for larger

arrays to the point that the flood images of neighboring channels in some areas have

considerable overlaps (see [118] and [119] for instance). A remedy to this is to employ a

digital multiplexing scheme for which ADC must be performed prior to multiplexing.

4.3.   Time-over-Threshold Readout Method

As mentioned in section 4.2.2, the main component of an MCA is the ADC that digitizes the signal according to its amplitude. Typical ADCs generate a 12-bit signal [22, 23] providing 4096 segments for digitization. However, transferring these 12 bits requires 12 cables and 12 input ports at the memory section. Another disadvantage is that in applications like PET in which the time resolution is of great importance, another component to determine the arrival time of the signal is required. Generally, SCA and MCAs utilize the leading-edge timing method or the zero-crossover method with 4-ns resolution [117]. This is inadequate in the case of TOF-PET. Furthermore, this ADC method cannot be applied before multiplexing since it generates 12 digital signals for a single channel, which is hard to propagate and process them in a digital multiplexer. And it is worth to remind that multiplexing is indeed performed to reduce the cables and ports.

A very simple but effective ADC is the time-over-threshold (ToT) method in which the duration of signal over a predefined threshold is recorded. Its design is very simple and compact since it employs only one comparator. The comparator output signals are all of the same amplitude (same as SCA) but different pulse widths. Figure 4.5 schematically depicts the comparator output signal for a sample of incoming pulses. Unlike SCA, the 1-bit output pulse still has energy information embedded in its pulse-width. In other words, this method employs another dimension of the signal to preserve its energy information. Besides, it does not require the energy window calibration; it suffices to adjust the threshold slightly over the noise level. Furthermore, the output signal carries both time and energy information, and hence there is no need for an additional timing component. The time resolution of typical ToT ASIC boards can be as short as 100 ps [30].
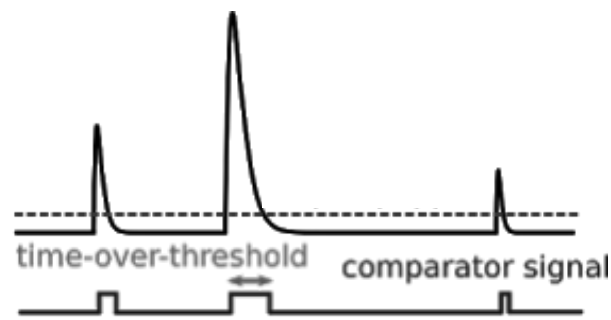
Figure 4.5. Basic concept of conventional ToT.

The great advantage of ToT method over the conventional ADC (used for MCA) is that it can be applied to all the channels individually for two outstanding reasons; firstly, it only generates a 1-bit signal, secondly, it has a very compact design in a sense that a large number of channels (48 or 64 channel in this presented work) can be converted over a small ToT ASIC board. Consequently, this enables digital multiplexing since a 1-bit digital signal can easily propagate through digital gates without any distortion.

Several modified ToT methods have been introduced in the literature to improve both energy and time resolution [30–35]. It is interesting to know that both PHA and ToT method each utilizes only one dimension of the signal; PHA takes the pulse-height, and ToT takes the pulse-width. Consequently, the modified ToT methods attempt to incorporate both information to make a protocol to generate output pulses with better energy and time resolution.

Grant and Levin proposed a dual-threshold ToT method for fast timing in coincidence detection, particularly for TOF-PET [30]. In this scheme, there are two compact comparators. One for the low threshold, as in the conventional ToT, which is set slightly above the noise level, and one for the high threshold which is set below the 511-keV photopeak. The duration of the signal from rising above the low threshold until falling

from the high threshold is recorded (see Figure 4.6). If the signal fails to cross the high threshold within a predefined delay time, the output pulse-width will be equal to the delay time and will be skipped by the processing unit.

Shimazoe *et al*. proposed the novel dynamic ToT method [31]. In this method, the threshold value for the comparator gets positive feedback from the input signal and increases slowly by using a simple RC integral circuit (RC ramping) until it meets the signal again. This duration is recorded as the ToT pulse (see Figure 4.7). The employment of the dynamic threshold significantly improves the energy resolution of the ToT method. This energy preservation makes this method a reasonable option for detection systems or imaging machines where energy discrimination is essential. In the study of collimator-based double photon imaging, which is presented in Chapter 6, the system must distinguish between 171-keV and 245-keV photons, and hence the dynamic ToT method is an apt choice for ADC.

Yonggang *et al*. proposed a more complex dynamic ToT scheme which requires first recording many output signals to define the dynamic threshold curve, and then a digital signal synthesizer to implement this curve as an analog time-varying voltage [32]. Kim *et al*. proposed a multi-ToT method in which the signal is fed to 4 ToT blocks with different threshold values [33]. The ToT pulses are then analyzed for energy and time resolution as well as positioning the origin of the signal within the detector array in case of multiplexed input signals. Orita *et al*. suggested that the ToT method can also be applied in current-mode readout schemes which results in a significant time resolution due to the low impedance and consequently a broad bandwidth [34]. This method provides a 50-ps FWHM time resolution that makes it a perfect choice for TOF-PET systems.
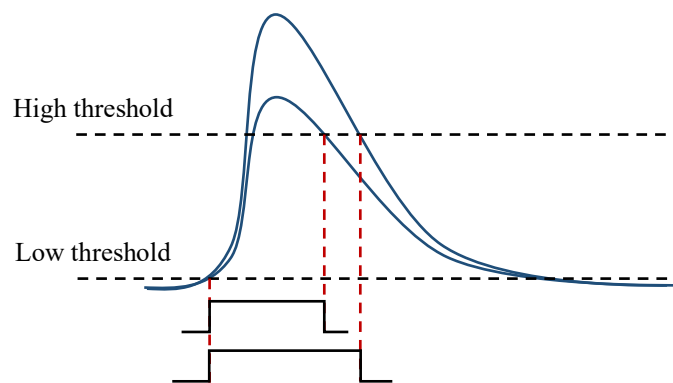
Figure 4.6. Dual threshold ToT scheme proposed by Grant and Levin [30].
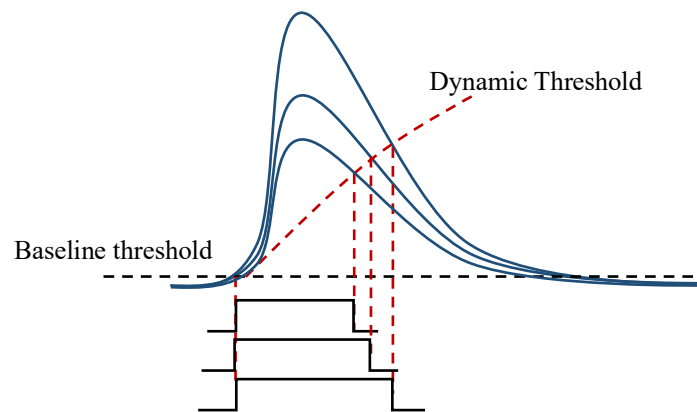
Figure 4.7. Dynamic ToT method proposed by Shimazoe *et al*. [31].

4.4.   Scanner Configuration

The ring of detectors in PET could be arranged in a circular or modular configuration. The modular PET shown in Figure 4.8 has certain advantages over the circular configuration. First of all, the scintillator crystals can be arranged in rectangular blocks which is easier than arranging them in a circular configuration. Secondly, the readout scheme is also modular, and each module has an individual readout circuit. Moreover, it is easier to change the size of the ring by simply adding more modules without changing the crystal arrangement and readout scheme.
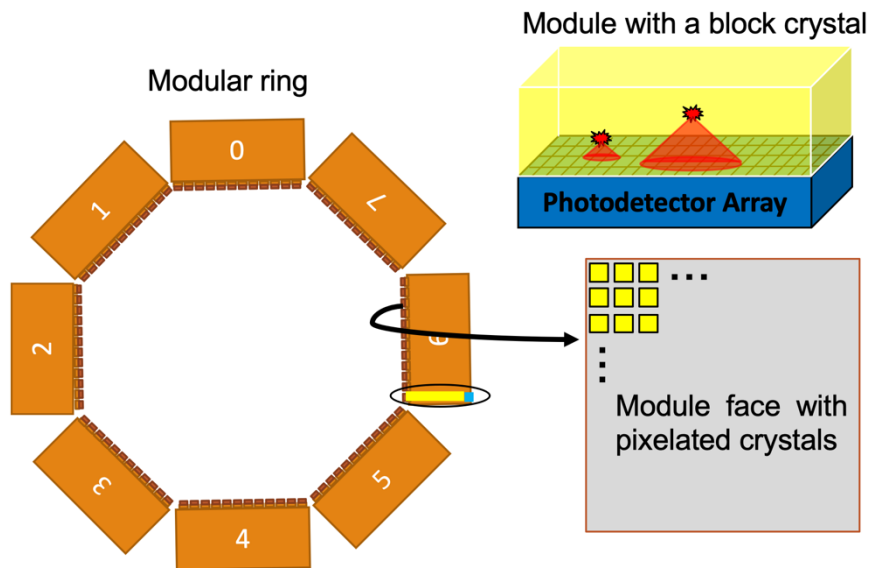
Figure 4.8. A modular PET system with pixelated crystal arrays or monolithic block crystals.

4.4.1. Detectors

In order to achieve 1-mm spatial resolution, the detector pitch must be 2 mm including the crystal width and reflector thickness. To this end, the crystal size of **1.6 × 1.6 × 15 mm³** was chosen to be covered with a 0.2-mm thick reflector.

Choice of crystal

Several factors must be kept in mind when choosing a scintillator crystal for PET imaging. First, the crystal must have enough stopping power to stop 511-keV photons. This depends on the density and the effective atomic number (Z_{eff}) of the crystal compound. The effective atomic number of a compound is the atomic number representing the attenuation properties of the compound. Scintillators with higher Z_{eff} are more likely to stop incident photons and hence they provide better γ-detection efficiency for a given length of the crystal.

Another important factor is the light yield or photon yield that is the total light produced through the scintillation process, which determines the energy resolution of the detector. The energy resolution is an important parameter for PET detectors because a scattered photon is no longer propagating in the opposite direction with respect to its pair and thus it must be discarded. The light yield is also an imperative factor for DOI-PET detectors, which is explained later.

Another factor is the scintillation decay time. When a γ photon interacts with the valance electrons in the crystal lattice, it takes time (typically in the picosecond range) to elevate the electrons to the conduction bands. This contributes to the intrinsic rise time of the scintillator. Then, a pretty long time is needed for the excited electrons to decay to the intermediate bands provided by the activator. This contributes to the intrinsic decay time of the scintillator, which can be as small as 600 ps for BaF_2 or as large as 1 μs for CsI:Tl. Such a long decay time can affect the performance of the detector by elongating the dead time of detection. Thereby it is not an apt choice for PET since the activity and thus the count rate is usually high. Particularly in TOF-PET, the timing precision in coincidence detection is essential, which limits the choice of scintillator crystal to those with short rise and decay time [121, 122].

A list of scintillator crystals used in PET detectors was provided in Table 3.1 in the previous chapter. Among all, Ce:GAGG has a relatively high density and effective atomic number (Z_{eff}) that facilitates the detection efficiency of the system. It has a light yield (57,000 photon/MeV) that provides a high intrinsic energy resolution. Therefore, it is a good choice for our system development, particularly its high light yield will come in handy for dual-ended readout with unpolished crystal which will be explained in the next chapter. Also, GAGG is not self-radiative. LSO, LYSO, LuAG, and LuAP that are

commonly used in PET developments are self-radiative due to the radioactivity of lutetium. Nevertheless, GAGG has a relatively high decay constant (88 ns) in comparison with other scintillators. This time constant could be decreased by increasing the percentage of the activator [123]. Kamada *et al.* [124] also proposed co-doping GAGG with cerium and alkali earth elements to improve its decay time. However, this characteristic is important only in TOF-PET systems which is not within the scope of this system.

Photodetector

In the past decade, SiPMs have been extensively used in PET detector developments thanks to their high sensitivity, high photon counting efficiency, good time resolution as short as a few picoseconds, their compact design, and being insensitive to the magnetic fields in hybrid PET-MRI systems. In this work, **KETEK PM1125 SiPM** array (12 × 12) with a pixel size of **1.6 mm** and a pitch of **2 mm** operating with -32.5 V was selected. The 1.6-mm pixel size provides us with a perfect individual coupling of crystal and SiPM. PM1125 has 25-µm-wide microcells which increases the quantum efficiency compared to the previous version (PM1150). The only drawback of this SiPM is that the active area of each pixel is 1×1 mm^2 which results in 60% loss of the scintillated light. The SiPM array and GAGG array is shown in Figure 4.9. The 0.4-mm gap between crystals was filled with BaSO$_4$ for optimum reflection of the scintillated light. The scanner is designed for small animal studies. Therefore, a small ring with a 70-mm diameter is plausible. To make this ring size, 8 modules of the SiPM-GAGG array are required to be arranged in an octagonal configuration shown in Figure 4.10.

ToT

(X & Y)

24 lines

× 8 modules

2 mm

Digital TOT
DAQ

1.6 mm

ToT

USB/SSD

24 lines

12 x 12

24mm
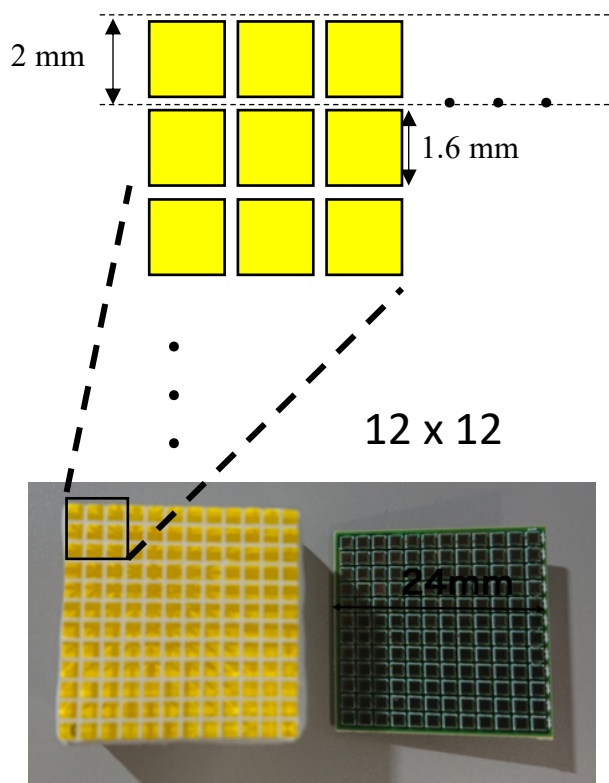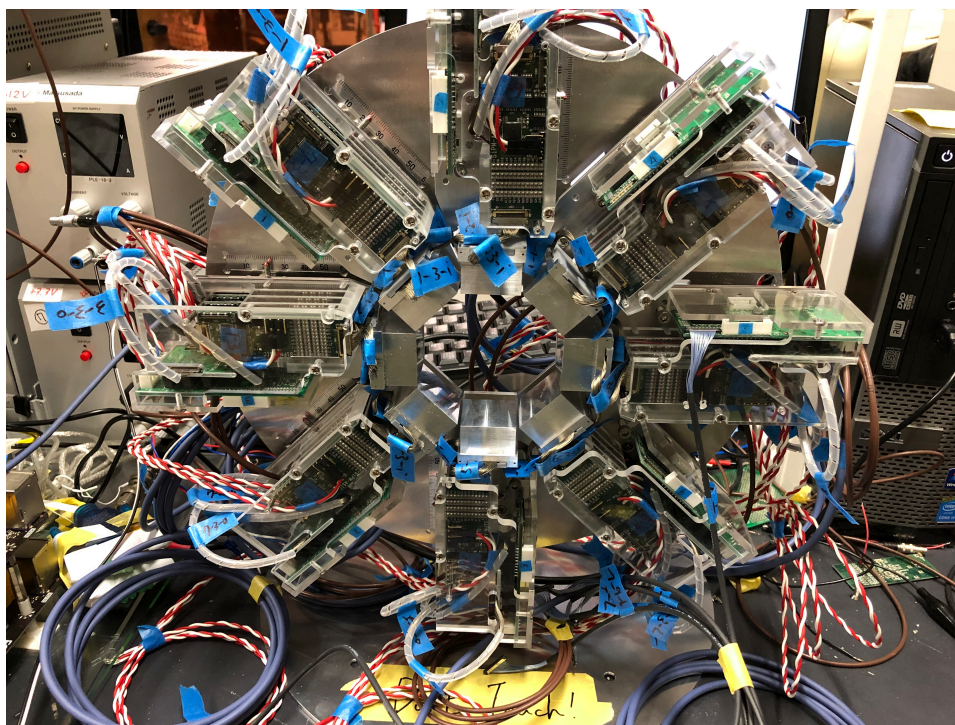
Figure 4.10. Animal PET scanner with 8 modules of 12 × 12 detector array.
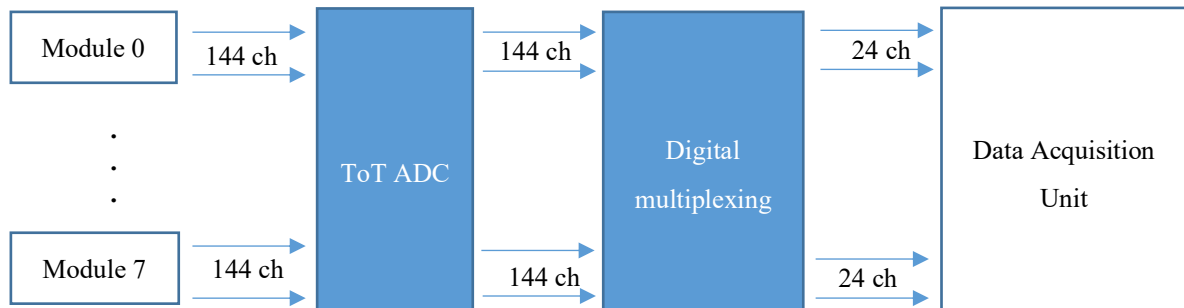
Figure 4.11. Readout scheme for fully digital data acquisition and processing.
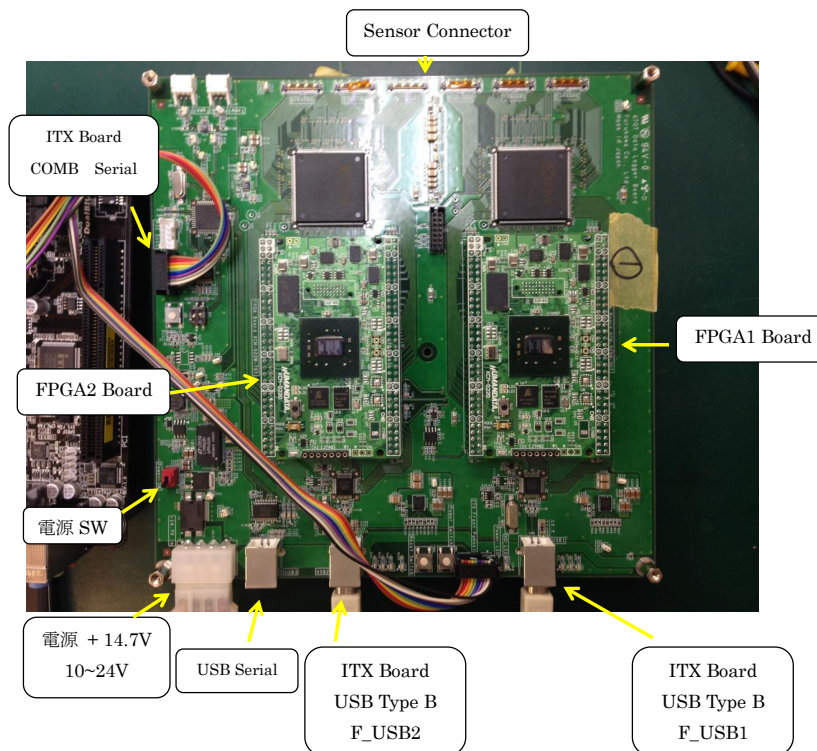
Figure 4.12. Data acquisition unit used for digital PET system.
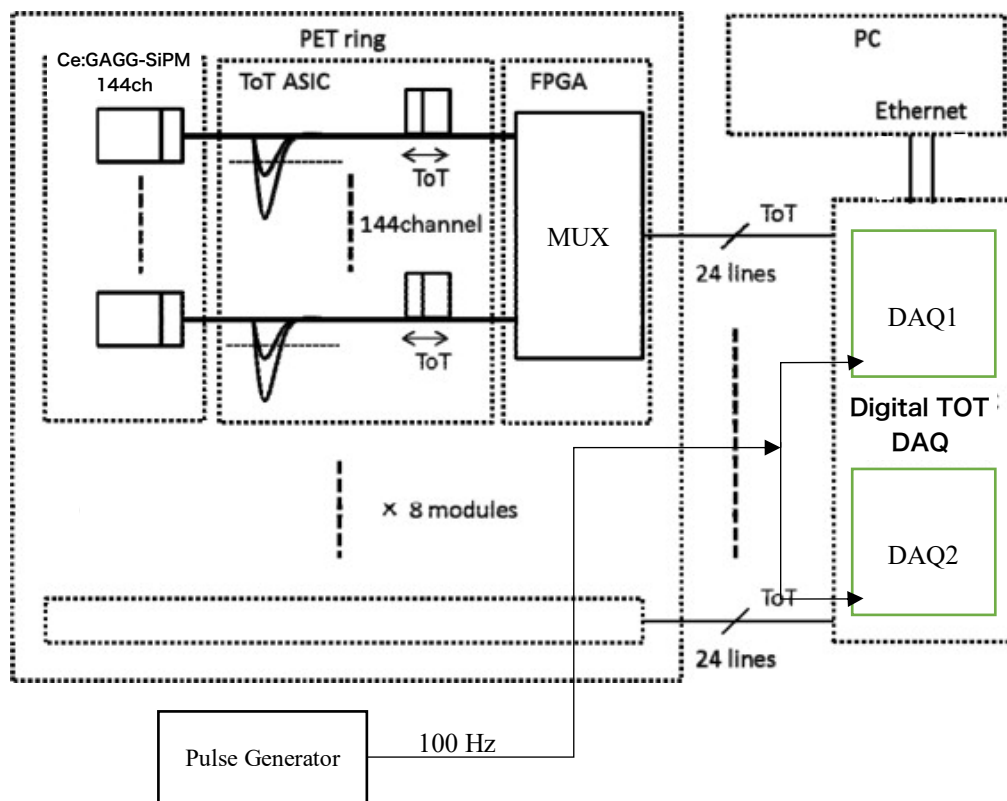
Figure 4.13. Digital readout configuration.

4.4.2. Digital Readout Scheme

One of the main objectives of this research is to develop a digital readout scheme for the high-resolution PET. The scheme is shown in Figure 4.11. As explained in section 4.3, the ToT method enables ADC prior to multiplexing which facilitates the digital multiplexing scheme. The 144 output channels of each module are connected to 3 ToT ASIC boards with 50-ps resolution operating with 2.5 V, and then connected to an FPGA to multiplex into 24 channels to connect to an input port of a data acquisition (DAQ) unit. The DAQ used in this system has a dynamic ToT data logger board consisting of 2 FPGA boards operating with a 400-MHz clock – equivalent to 2.5 ns time resolution – to collect data and an AMD® E1-2100 (1.0 GHz) CPU to process the data (Figure 4.12). Two DAQs

were used since each has only 6 input ports. Therefore, 4 modules were connected to each DAQ, and a synchronization pulse was sent to both DAQs. Figure 4.13 shows the schematic view of the readout configuration. The acquired data were analyzed with time fixing and demultiplexing to extract coincidences and reconstruct the image.

4.4.3. Experimental Setup

A set of experiments were performed in the radioisotope center using ^{18}FDG, ^{22}Na, ^{133}Ba, and ^{57}Co sources. In all experiments, PET ring and DAQs were placed in a chamber under 20°C temperature and 35% humidity. Background activity was also measured and was affirmed that the background activity was low.

4.5. Results and Discussion

During measurements, the threshold value controller of many channels stopped functioning, and hence it was no longer possible to adjust the optimum threshold for them. This could have happened due to applying a higher voltage for writing the value, applying a higher operating voltage for a long time, or short-circuit between one board to the supply pin of the board behind in the arrangement. Therefore, to have a balanced performance we let all the channels work with the default threshold, and as a consequence energy resolution was poor. In order to calibrate for the energy window, the right-side value of FWHM of the 133Ba spectrum was chosen as an energy threshold for the incidents with 511 keV energy (Figure 4.14). To be assured that the problem is from ASIC boards, the pulse-height spectra of several channels were recorded by using an MCA. The spectrum by MCA had a clear photopeak for 511 keV emission of ^{22}Na (Figure 4.15).
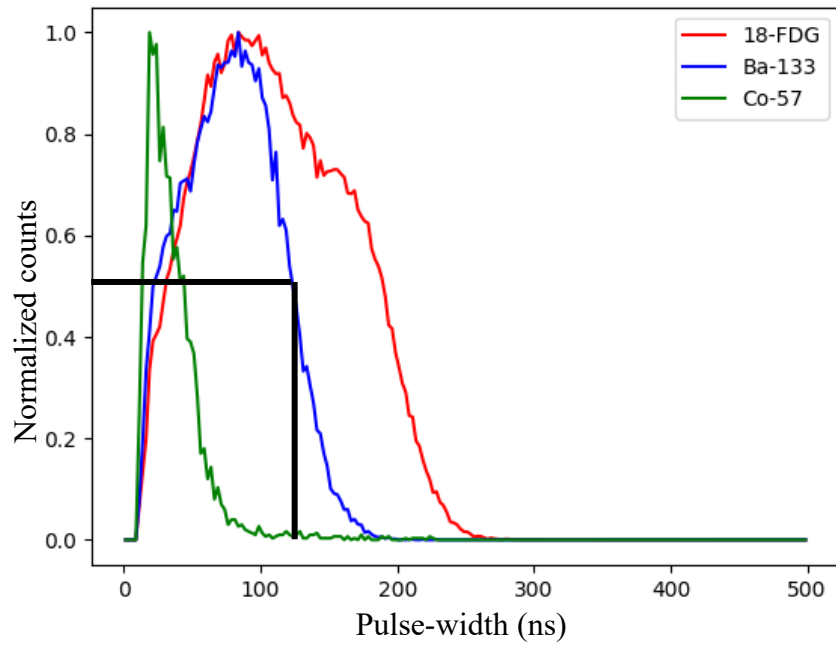
Figure 4.14. Pulse-width spectra of ^{18}FDG (511-keV), ^{133}Ba (302~356 keV), ^{57}Co (122~136 keV) from a selected detector. Due to the unset threshold values, photopeak is not seen. Therefore, the right side half-maximum value of the ^{133}Ba spectrum is used as a threshold to skip low energy events.
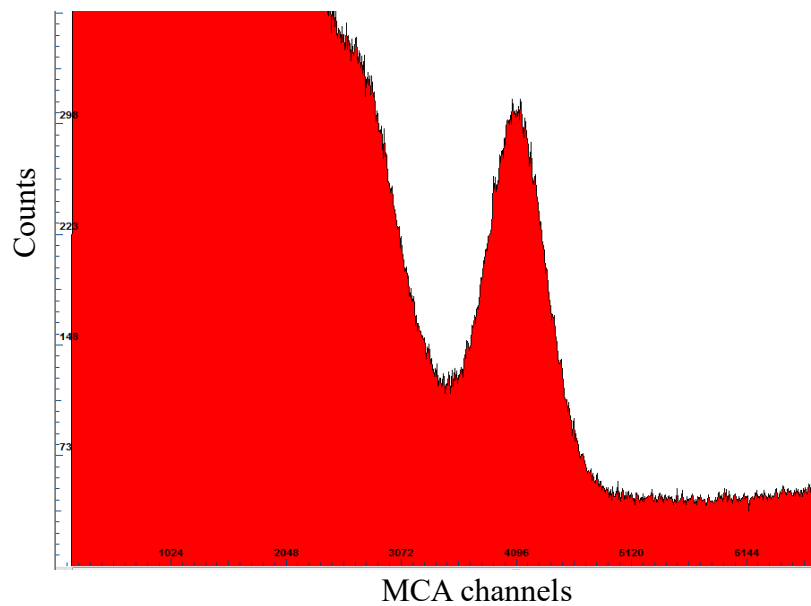
Figure 4.15. Pulse-height spectrum of the selected channel acquired by an MCA.

Figure 4.16 shows the coincidence time of the detected coincidences by a selected pair of facing detectors. The histogram was fitted with a gaussian curve with ~ 12.5 ns FWHM. This means that the system is still capable of detecting coincidences with a coincidence time window of ~ 15 ns which is comparable to other reported PET systems [125] even though detectors do not show good energy resolution.

After setting the time window, coincidence data was extracted and implemented in an MLEM algorithm to reconstruct the image. Figure 4.17 depicts the reconstructed image of a 22Na point-source with a 0.7mm diameter positioned roughly in the center of the ring. The point is reconstructed with 1.07 ~1.21 mm resolution. In brief, a small animal PET scanner with a ~ 1-mm spatial resolution was developed with ToT front-end ASIC and fully digital data acquisition. The system performance was evaluated, and a spatial resolution of 1.14 mm was achieved in the center of FOV. In order to gain the best performance from the system, the threshold values for ToT ASICs must be optimized individually for each detector channel.
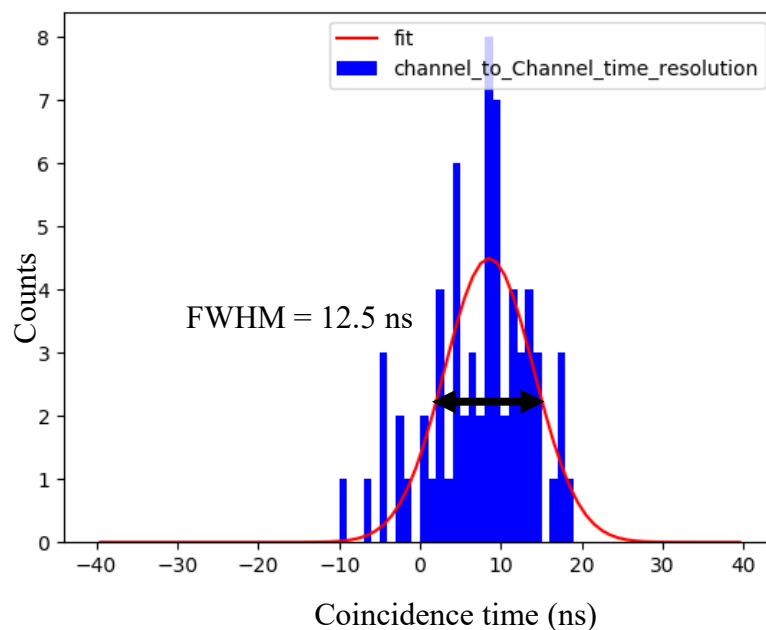
Figure 4.16. Coincidence time resolution between a selected pair of facing detectors.
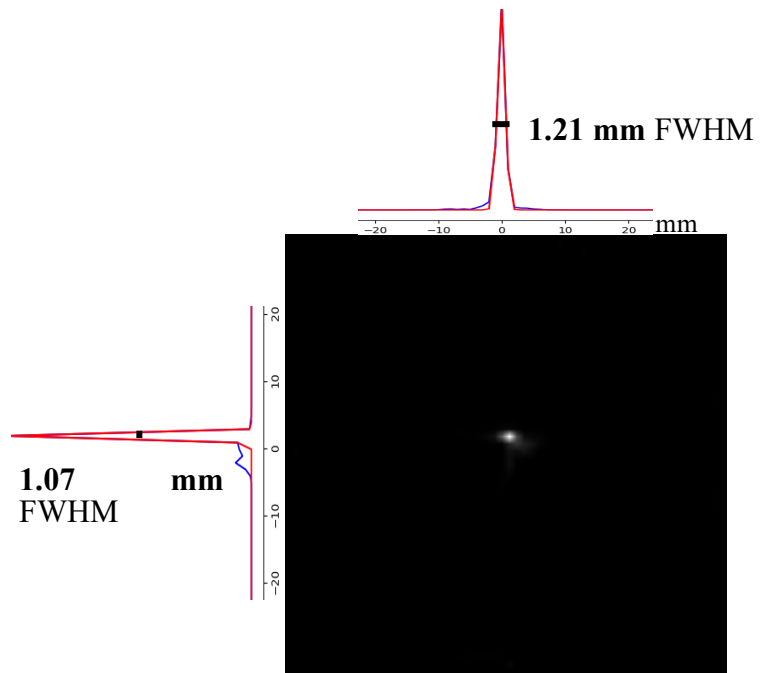
Figure 4.17. Reconstructed image of a 0.7mm 22Na source using MLEM algorithm (10 iteration).

5. DUAL-ENDED READOUT FOR SUBMILLIMETER PET IMAGING

Parallax error is quite significant in small animal PET systems and it should be resolved for the future system development since it is more severe for a system with finer pitch. The remedy for this error is depth of interaction identification which is explained in this chapter with common methods in the literature. The most effective method for pixelated arrays is the dual-ended readout method. A great advantage of this method is that it can be implemented with a full digital readout system. The materials and methods for this study are presented in section 5.3. The results of this work help us to make the right choice of surface roughness for the crystal to be assembled in the modules and final PET ring with the 1.36-mm detector pitch in the next small animal PET system.

5.1. Parallax Error in PET Images

In the previous chapter, the factors that affect the spatial resolution of a PET system were described and formulated in equation (4.1). However, this equation is insufficient to describe the spatial resolution of a PET system. This equation is valid only for the center of the ring. The spatial resolution in other regions of FOV is completely different. Figure 5.1 figuratively demonstrates how and why spatial resolution varies in the FOV. The reason simply arises from the length of crystals contributing to the uncertainty associated

with the LORs. When the activity is in the center of the ring, coincidences always involve facing detectors. Consequently, the corresponding LORs would have uncertainty as wide as the detector pitch, resulting in half-pitch FWHM resolution in the center. However, when the activity is off-center, since annihilation photons could have interacted at any depth inside the crystals, the whole contour of the crystals contributes to the uncertainty, making much wider LORs. This is called parallax error and increases radially in the FOV.

Xia *et al*. [7] modified equation (4.1) into the following equation in order to include parallax error:

$$\Gamma = a \sqrt{\left(\frac{d}{2}\right)^2 + \frac{|l^2 - d^2|}{D^2}s^2 + (0.0022D)^2 + r^2 + b^2} \qquad (5.1)$$

where *l* is crystal length and *s* the radial distance from the center of the ring.
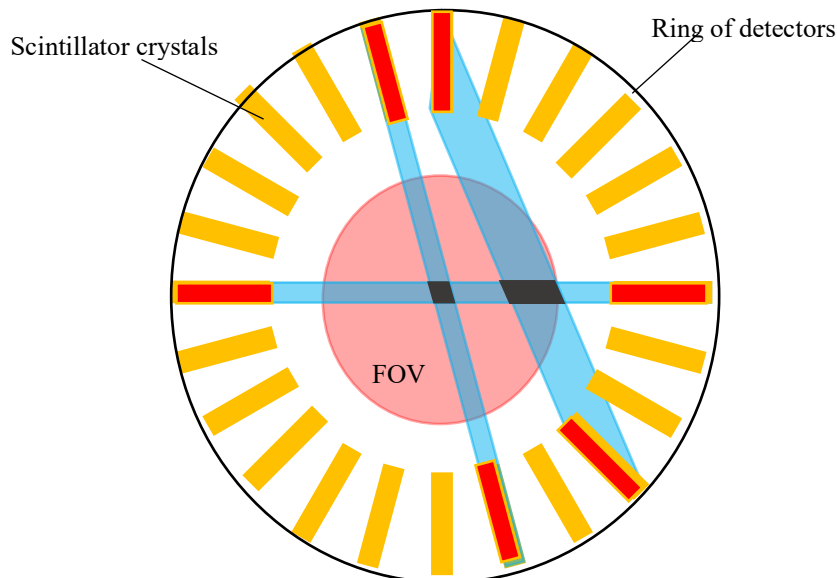

Figure 5.1. Origin of parallax error in PET images.
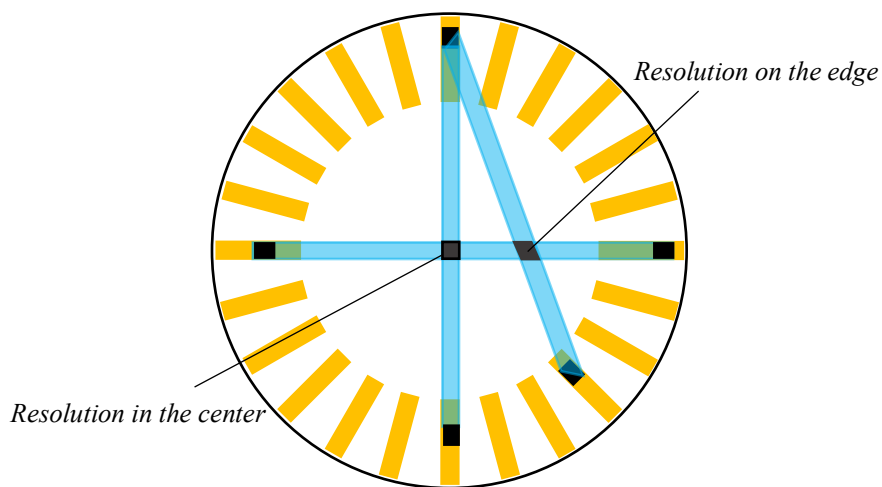
Figure 5.2. Figurative illustration of how DOI improves spatial resolution in PET.
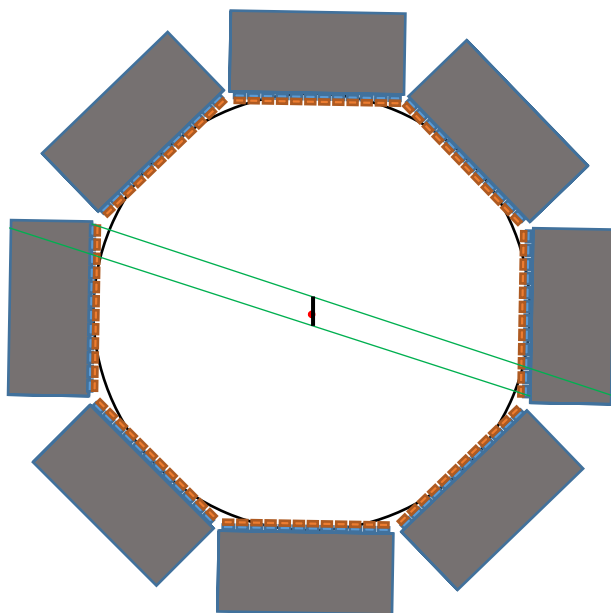
Figure 5.3. Effect of modular configuration on LOR and consequently spatial resolution in PET.

5.2.   Depth of Interaction

Resolving parallax error requires positioning of the incident photons in the 3rd dimension; through the length of crystals. In a nutshell, the depth of interaction of the incident photons in the crystals must be extracted. If this positioning has the same resolution (certainty) as of the positioning in the other two dimensions, the parallax error will be eliminated from the image. This can be seen figuratively in Figure 5.2. In fact, in equation (5.1), one would substitute DOI resolution, *w*, for *l*;

$$\Gamma = a\sqrt{\left(\frac{d}{2}\right)^2 + \frac{|w^2 - d^2|}{D^2}s^2 + (0.0022D)^2 + r^2 + b^2} \qquad (5.2)$$

In modular configurations for PET detectors in the ring, there is another small error as a result of non-circular configuration, which is shown in Figure 5.3. DOI resolution eliminates this error as well and improves the spatial resolution of the image in a way that spatial resolution will become more uniform all over the image.

DOI information also improves the time and energy resolution of the system. For the time resolution, the arrival time of scintillated photons slightly varies according to the depth of interaction and is averaged over the length of crystal in absence of DOI information [121, 122, 126]. With DOI information available, the arrival time of scintillated photons is averaged over a segment of the crystal. In the same way, the amount of light collected at the photodetector, which determines the energy of the incident photon, depends on the depth of interaction. With DOI information available this is averaged over a segment of the crystal, providing sharper energy resolution. Both time and energy resolution can be calibrated for various depths of the crystal during DOI calibration.

5.2.1. DOI Estimation Methods

Monolithic block crystal with 3D positioning

Monolithic block crystals have been used in gamma imaging since the invention of the so-called scintillation camera by Hal Anger [52, 120]. Even though pixelated crystals were developed for better positioning accuracy, the ease of fabrication and assembly still kept monolithic blocks in use since the alignment of pixelated crystals on PMT pixels is a tedious job and requires high precision particularly for detectors with a relatively small pitch. In systems with monolithic blocks, the bulk crystal is coupled to an array of PMTs as shown in Figure 5.4. The scintillated light is shared by all the pixels in PMT array; however, due to the difference in solid angles and distance from point of interaction (knowing that light has attenuation in the crystal), pixels right below the interaction point would have larger outputs. By using some statistical methods, the 2D position of interaction is estimated. By the same token, the vertical position of interaction could be estimated. Statistical methods, in general, require a large amount of memory and complex algorithms to trace back the origin of interaction [127, 128]. An alternative method is to employ neural networks that were first applied to 2D positioning in 1996 by Delorme *et al*. [129], and two years later to 3D positioning by the same group (Clément *et al*.) [130].

Despite all the advancements in mathematical algorithms and instrumentation to increase the accuracy of positioning the origin of scintillation, PET scanners with monolithic blocks fail to provide theoretical spatial resolution as discussed before. Moreover, these advancements require excess costs on electronic devices and memories. Particularly with recent precision in crystal array fabrication and alignment, the use of crystal arrays is becoming more widespread in the field.
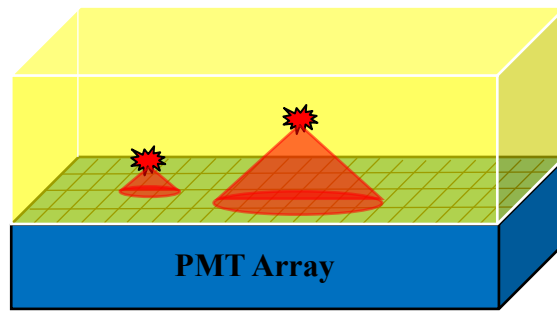
Figure 5.4. Light sharing method for a monolithic block crystal coupled to a PMT array

Multilayer scintillators

The monolithic block crystal was pixelated in 2D with an array of long, narrow crystals to provide considerably accurate 2D positioning within the block. In the same way, one may think of pixelating the crystal in the 3rd dimension as well. This is the basic idea of multilayer scintillator crystals. However, inserting a PMT array for each layer is not practical and hence PMT array remains 2D at the bottom crystal array. Therefore, some practical implementation is required.

One simple idea is shown in Figure 5.5 in which a stack of two identical crystals with a gap in between is used [131]. The gap makes turbulence in the propagation of the scintillated light. As a consequence, the output signal would have different rise time and decay time depending on the layer where the incident photon interacted. The crystal may be split into more layers to increase the DOI positioning accuracy; however, there is always uncertainty in the positioning the original layer of interaction since the difference in the output signals is considerably small.

In order to increase the contrast in the rise time and decay time of output signals depending on the layer of interaction, the phoswich (phosphor sandwich) concept is

recommended; the idea that was introduced a long time ago (Wilkinson 1952, [132]). In this scheme as shown in Figure 5.6, two (or more) layers of crystals with different timing performance are used [133]. It could be either two different scintillators or two identical scintillators but different percentages of activator (doping).

Even though the phoswich detectors show better DOI capability than the stacked identical layers, the DOI resolution is still limited to the number of layers, and fabricating crystals with more than 5 layers is quite impractical. Nagarkar *et al*. [134] proposed the continuous concept of phoswich in which the percentage of doping varies continuously through the length of the crystal. The idea is fascinating; however, the fabrication of such crystals has its own complications in crystal growth.
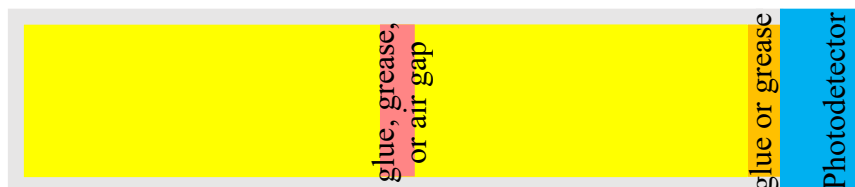

Figure 5.5. The idea of stacked crystal for multilayer scintillation detector [131].
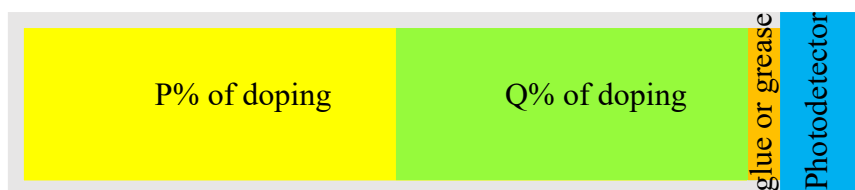
Figure 5.6. Concept of phoswich (phosphor sandwich) scintillation detector.

Another multilayer array scheme is fabricating a 3D array of identical crystals separated from each other by air gaps and reflectors in a way that the scintillated light is guided to a number of PMTs [135]. By employing some algorithms, the origin of scintillated light can be traced back. This method also has complications in assembling and aligning the crystals in the array as well as in the signal processing to estimate the position of interaction. Moreover, DOI resolution in this method is again limited to the number of layers in the array.

Wavelength discrimination method

In some crystals, e.g. GAGG, the absorbance spectrum has a transition that overlaps with their emission spectrum. This is shown in Figure 5.7 for GAGG crystal. This means scintillated photons with shorter wavelengths have short absorption length and thus dissipate in the crystal unless the interaction point is close enough so that they could reach to PMT. In early studies we used this feature to estimate DOI [136, 137]. However, there is no photodetector able to discriminate the wavelength of scintillated photons. One possible solution to utilize this feature as we described in [136, 137] is to couple the crystal to a pixelated PMT where a sharp cut filter is attached on half of the pixels. Pixels covered with the optical filter are connected together to make one output signal, and other pixels are connected together to make another output signal. The ratio of filtered PMTs to non-filtered ones is a measure to estimate DOI. However, DOI resolution in this method is not sufficient since the sharp cut filters are not perfect and also there is always crosstalk between PMT pixels.

Dual-ended readout

A very simple but effective method that has been studied in the past two decades is the dual-ended readout method [8–14] in which two photomultipliers are coupled to the top

and bottom of a single crystal as shown in Figure 5.8. The ratio of one output to the sum of outputs gives information regarding the position of interaction. In recent studies on the dual-ended readout detectors, less than 2-mm DOI resolution was achieved [9, 138, 139]. This fine resolution is difficult to achieve with multilayer crystals and 10 layers of crystals are required in fabrication, which is not feasible. Indeed, a great advantage of the dual-ended method is that it is applied to a single continuous layer of crystal and thereby it has no physical limitation as in multilayer schemes.
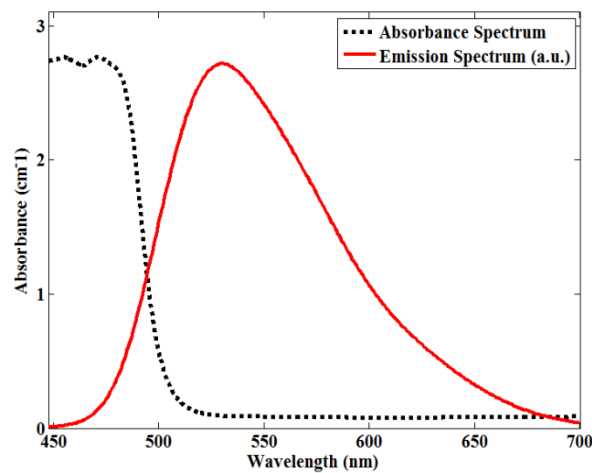
Figure 5.7. Absorbance and emission spectra of Ce:GAGG crystal.
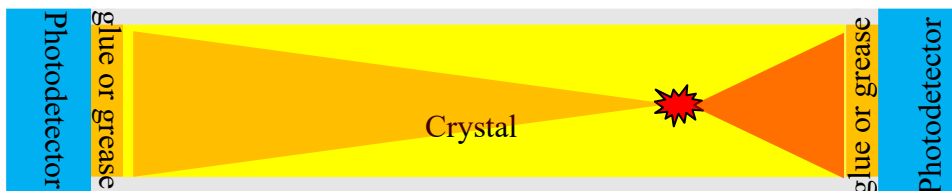
Figure 5.8. Dual-ended readout detector for DOI identification.

Fig. 2. DOI-dependency of spectra of detected photons seen by spectrometer.

6. COLLIMATOR BASED DOUBLE-PHOTON IMAGING

The readout system for this method is of great importance. Since photons with different energies must be detected, the readout scheme must preserve the energy resolution of the original signal. To this end, a dynamic ToT-based readout was applied and evaluated in the experiments.

6.1. Method and Materials

6.1.1. Readout

The signals were readout through a 64-channel dynamic ToT board that preserves the high energy resolution of the detectors to extract 171 keV and 245 keV incidents. Data was stored in a DAQ unit with 2.5 ns resolution described in Chapter 4 (Figure 4.12).

6.2. Experiments and Results

6.2.1. Energy and Time Calibration with dToT

One of the concerns in this study is designing a full digital readout system with ToT method. In this part of research, the dynamic ToT concept [31] was used since the energy of target photons are different and thus the energy resolution is of great importance.

Preliminary measurement with a 1-MBq ^{111}In source was done to evaluate the method. The source was prepared at the bottom of a microtube with a 2-mm diameter at the bottom and a 4-mm diameter at the top. The focal point was set on the center of the source and data was recorded in 12 hours to calibrate for energy (pulse-width) window and coincidence time window.

Figure 6.1 shows the pulse-width spectra of a sample channel. Even the photopeak for X-ray emission from electron capture can be observed. We can compare this energy response with that of PET detectors with normal ToT in Chapter 4. This vast difference comes from the size of crystals, the active area of SiPM pixels, and the ToT methods.
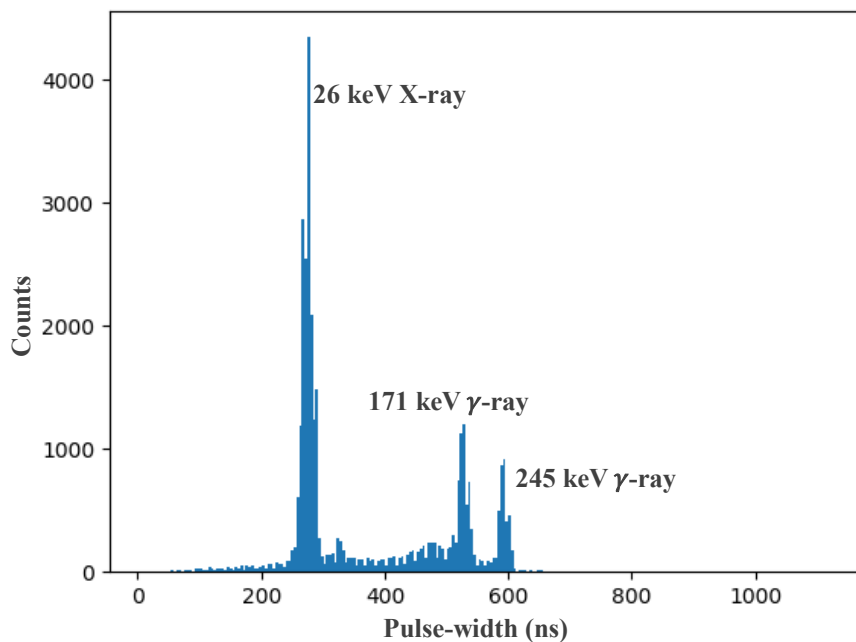
Figure 6.1. Pulse-width spectra from a sample channel.

6.3.   Discussion

The detector module combined with the dToT method provides an excellent energy response enabling the discrimination of X-ray emission, 171-keV, and 245-keV peaks required for proper coincidence detection. In PET, only 511-keV is emitted and the system could work even with poor energy resolution, as shown in Chapter 4. However, in DPECT, energy resolution is of great importance and normal ToT is not a proper readout scheme. Therefore, the dynamic ToT was applied.

7. DISCUSSION AND CONCLUSION

This research was particularly done towards developing high-resolution coincidence imaging systems (PET and DPECT) with full digital readout schemes using time-over-threshold (ToT) methods. Particularly in PET, since the trend is reducing the detector pitch and implementing the dual-ended readout for DOI identification, the number of channels is increasing generation by generation. In Chapter 4, it was explained that why individual readout is necessary in order achieve sub-mm resolution. The conventional multiplexing network limits the spatial resolution to 1-mm and no further improvement can be done by reducing the crystal size – since in such a case b is ~ 1.1 mm in equation (4.1). Quantitively speaking, for a system with 2-mm pitch pixelated detectors and conventional multiplexing scheme (electronic encoding, $b = 1.1$), the spatial resolution in the center of the ring is ~ 1.5 mm, while 1-mm resolution is expected from 2-mm detector pitch.

On the other hand, reading out the large number of channels without multiplexing is not feasible. With the conventional ADC approach, each channel will be digitized in 12 bits which multiplies the number of outputs by 12. ToT is an alternative ADC method that provides a single-bit output for each channel. It is also very compact since it has only one comparator. Therefore, it can be implemented for a large number of channels on a small

ASIC board. Since each channel has only one-bit signal, digital multiplexing is feasible, and it does not make any distortion in demultiplexing because the signal is encoded digitally and decoded in the data processing. Sometimes, miscoding happens due to some noise or pulses from neighboring channels. In such cases, that pulse cannot be decoded, and it will be skipped, and therefore, it does not lead to mispositioning of the original detector. In this sense, this readout scheme is robust against noise.

The proposed readout scheme was tested in a smaller scale (smaller number of channels) first. A modular PET system with 2-mm detector pitch was assembled. Each module was 12×12 detector array (144 channels). Even though the ToT ASICs were partially broken, and the threshold level could not be adjusted (leading to very poor energy resolution), the data was recorded, decoded, coincidence data was extracted, and a ~ 1-mm spatial resolution was assessed in the center of the ring.

Next step was reducing the detector pitch for next digital animal PET system with sub-mm resolution. The pitch should be around $\sqrt{2}$ so that within the same dimensions the number of channels will be twice. KETEK GmbH manufactures SiPM arrays (PM1125) with 1.36-mm pitch which is close to $\sqrt{2}$. This can provide 0.7 mm spatial resolution in the center of the ring, however, in order to develop a submillimeter PET imager, it is essential to apply a DOI method to the system. Since the detector has smaller pitch and longer length (for better detection efficiency), parallax error is more severe. In the 2-mm system the spatial resolution at the edge of FOV is ~ 4 mm (at center ~ 1 mm), while in the 1.36 mm system, it is ~ 6 mm (at center 0.7 mm).

Another issue is the ToT method. In the 2-mm system, the energy of the signals was not of great importance and normal ToT could still provide good digital signals. However, since DOI identification in dual-ended method is done by comparing the energy of the

two outputs, it is important to preserve the energy of the signals. Therefore, normal ToT is not a good choice. Slew-rate ToT method could be an option that is going to be evaluated with the 2-mm system. Dynamic ToT (dToT) is another alternative since it can provide a linear response over a vast range of energies. In other words, ToT pulse-width generated by dToT is proportional to the energy of the analog signal over a wide range. Therefore, it can preserve the contrast between outputs and hence the DOI resolution of the detector.

In order to show the great capability of this digital readout method in energy preservation, the performance of a collimator-based double-photon imager coupled to a dynamic ToT board for digital readout was evaluated. In DPECT, energy resolution is of a great importance since photons with different energies are emitted. The collimator-based DPECT itself is a new imaging modality. Its concept and the preliminary design of the collimator was discussed in Chapter 6. Possible radionuclides with double photon emission were introduced and the system was used to scan an ^{111}In source. Results show a very good energy response in the sense that even 26-keV X-ray emission can be distinguished thanks to the great energy preservation of capability of the dToT method. However, further optimization of design is required to achieve a reliable image. Particularly, the coincidence count rate was too low in this experiment. Only 64 central holes of the collimator were coupled to detectors. If all 256 holes are covered with detector, the coincidence count rate increases by a factor 16. Also, the size of the collimator could be expanded to introduce more channels and increase the solid angle coverage. Doubling the dimensions (2D) increases the coincidence count rate by a factor 16. The focal distance of the collimator (70 mm) is too long for animal studies where 30 mm is enough. Another parameter to be optimized is the collimator thickness which was

30 mm in this current design. A 20-mm thickness is enough in the case of ^{111}In to stop 171-keV and 245-keV photons. The latter two modifications together reduce the distance of the detector plane to the focal point to half (from 100 mm in current design to 50 mm), which increases the coincidence count rate by a factor 16. It should be noted as well that the source activity was 1 MBq, while in animal studies 40-50 MBq is generally used, which means 40-50 times better count rate.

All these measurements and investigations will lead to a digital animal DOI-PET aiming at sub-mm resolution currently under development. Two important components of this system are dual-ended detectors and digital readout. The digital readout component must preserve this DOI capability. The finer pitch along with implementing dual-ended detectors increases the number of channels by factor 4 which brings up the need for ToT readout method. The proposed digital approach is excellent in encoding and decoding the signals, however, the challenge is energy resolution of the method. In order to preserve DOI capability of the detectors, the readout system must preserve energy resolution, and to this end slew-rate ToT method is under investigation, as well as dynamic ToT method that was evaluated for DPECT system.

Bibliography

[1] E. Caroli, J. B. Stephen, G. Di Cocco, L. Natalucci and A. Spizzichino, "Coded aperture imaging in X- and gamma-ray astronomy," *Space Sci. Rev.,* vol. 45, p. 349–403, 1987.

[2] K. Van Audenhaege, R. Van Holen, S. Vandenberghe, C. Vanhove, *et al.*, "Review of SPECT collimator selection, optimization, and fabrication for clinical and preclinical imaging," *Med. Phys.,* vol. 42, no. 8, pp. 4796-4813, 2015.

[3] Y. Yoshihara, K. Shimazoe, Y. Mizumachi and H. Takahashi, "Evaluation of double photon coincidence Compton imaging method with GEANT4 simulation," *Nucl. Inst. Meth. Phys. Res. A,* vol. 873, pp. 51-55, 2017.

[4] K. Shimazoe, M. Uenomachi, Y. Mizumachi, H. Takahashi, *et al.*, "Double photon emission coincidence imaging using GAGG-SiPM pixel detectors," *J. Inst.,* vol. 12:C12055, 2017.

[5] S. E. Derenzo, W. W. Moses, R. H. Huesman and T. F. Budinger, "Critical instrumentation issues for <2 mm resolution, high sensitivity brain PET," *Elsevier Science Publishers,* pp. 25-37, 1993.

[6] R. Lecomte, "Technology challenges in small animal PET imaging," *Nucl. Inst. Meth. Phys. Res. A,* vol. 527, p. 57–165, 2004.

[7] Y. Xia, T. Ma, Y. Liu, S. Wang and Y. Shao, "A modified spatial resolution formula for DOI-PET," *IEEE Nucl. Sci. Conf. R.,* pp. 2632-2635, 2011.

[8]   L. Zheng, K. Shimazoe, Y. Yoshihara, A. Koyama and H. Takahashi, "Development of a dual-sided readout DOI-PET detector using 500-μm-pitch 64-ch SiPMs," *J. Inst.,* vol. 14:C04001, 2019.

[9]   Z. Kuang, X. Wang, X. Fu, N. Ren, *et al.*, "Dual-ended readout small animal PET detector by using 0.5 mm pixelated LYSO crystal arrays and SiPMs," *Nucl. Inst. Meth. Phys. Res. A,* vol. 917, pp. 1-8, 2019.

[10] E. P. Delfino, S. Majewski, R. R. Raylman and A. Stolin, "Towards 1mm PET Resolution Using DOI Modules Based on Dual-Sided SiPM Readout," *IEEE NSS/MIC ,* pp. 3442-3449, 2010.

[11] A. Kishimoto, J. Kataoka, T. Kato, T. Miura, *et al.*, "Development of a Dual-Sided Readout DOI-PET Module Using Large-Area Monolithic MPPC-Arrays," *IEEE Trans. Nucl. Sci.,* vol. 60, no. 1, pp. 38-43, 2013.

[12] S. Seifert and D. Schaart, "Improving the time resolution of TOF-PET detectors by double-sided readout," *IEEE Trans. Nucl. Sci.,* vol. 62, no. 1, pp. 3-11, 2015.

[13] H. G. Kang, G. B. Ko, J. T. Rhee, K. M. Kim, *et al.*, "A Dual-Ended Readout Detector Using a Meantime Method for SiPM TOF-DOI PET," *IEEE Trans. Nucl. Sci.,* vol. 62, no. 5, pp. 1935-1943, 2015.

[14] L. Guo, J. Tian, P. Chen, S. E. Derenzo and W. S. Choong, "Improving timing performance of double-ended readout in TOF-PET detectors," *J. Inst.,* vol. 15:P01003, 2020.

[15] S. Siegel, R. W. Silverman, Y. Shao and S. R. Cherry, "Simple Charge Division Readouts for Imaging Scintillator Arrays using a Multi-Channel PMT," *IEEE Trans. Nucl. Sci. ,* vol. 43, no. 3, pp. 1634-1641, 1996.

[16] M. Janecek, J.-P. Walder, P. J. McVittie, B. Zheng, *et al.*, "A High-Speed Multi-Channel Readout for SSPM Arrays," *IEEE Trans. Nucl. Sci.,* vol. 59, no. 1, pp. 13-18, 2012.

[17] M. Georgiou, S. David, E. Fysikopoulos and G. Loudos, "Development of a SIPM based gamma-ray imager using a Gd3Al2Ga3O12:Ce (GAGG:Ce) scintillator array," *IEEE NSS/MIC Seoul,* pp. 1-3, 2013.

[18]   E. Downie, X. Yang and H. Peng, "Investigation of analog charge multiplexing schemes for SiPM-based PET block detectors," *Phys. Med. Biol.,* vol. 58, no. 11, p. 3943–3964, 2013.

[19]   F. Boisson, V. Bekaert, J. Sahr and D. Brasse, "Description and properties of a resistive network applied to emission tomography detector readouts," *Nucl. Inst. Meth. Phys. Res. A,* vol. 872, pp. 100 - 106, 2017.

[20]   P. Després, W. C. Barber, T. Funk, M. McClish, *et al.*, "Modeling and Correction of Spatial Distortion in Position-Sensitive Avalanche Photodiodes," *IEEE Trans. Nucl. Sci.,* vol. 54, no. 1, pp. 23 - 29, 2007.

[21]   T. Zhao, B. Li, C. Li, R. Wang, *et al.*, "New Distortion Correction Algorithm for Two-Dimensional Tetra-Lateral PositionSensitive Silicon Photomultiplier," *IEEE Electron Device Letters,* vol. 38, no. 2, pp. 228-231, 2017.

[22]   M. Streun, G. Brandenburg, H. Larue, E. Zimmermann, *et al.*, "A PET system with free running ADCs," *Nucl. Inst. Meth. Phys. Res. A,* vol. 486, pp. 18-21, 2002.

[23]   W. Gao, D. Gao, C. Hu-Guo, T. Wei and Y. Hu, "Design and Characteristics of an Integrated Multichannel Ramp ADC Using Digital DLL Techniques for Small Animal PET Imaging," *IEEE Trans. Nucl. Sci.,* vol. 58, no. 5, pp. 2161 - 2168.

[24]   K. Shimazoe, Y. Wang, H. Takahashi, K. Kamada, *et al.*, "Time over Threshold based digital animal PET (TODPET)," *IEEE NSS/MIC,* pp. 3267-3271, 2011.

[25]   S. Gundacker, E. Auffray, B. Frisch, H. Hillemanns, *et al.*, "A Systematic Study to Optimize SiPM Photo-Detectors for Highest Time Resolution in PET," *IEEE Trans. Nucl. Sci.,* vol. 59, no. 5, pp. 1798-1804, 2011.

[26]   K. Shimazoe, T. Orita, Y. Nakamura and H. Takahashi, "Time over threshold based multi-channel LuAG-APD PET detector," *Nucl. Inst. Meth. Phys. Res. A,* vol. 731, pp. 109-113, 2013.

[27]   K. Shimazoe, H. Takahashi, K. Kamada, A. Yoshikawa, *et al.*, "Development of a prototype of time-over-threshold based small animal PET scanner," *Nucl. Inst. Meth. Phys. Res. A,* vol. 753, pp. 84-90, 2014.

[28]   C.-M. Chang, J. W. Cates and C. S. Levin, "Time-over-threshold for pulse shape

discrimination in a time-of-flight phoswich PET detector," *Phys. Med. Biol.,* vol. 62, no. 1, p. 258–271, 2017.

[29] M. Yoshino, K. Kamada, Y. Shoji, A. Yoshikawa, *et al.*, "Development and performance evaluation of Time-over-Threshold based digital PET (TODPET2) scanner using SiPM/Ce:GAGG-arrays for non-invasive measurement of blood RI concentrations," *J. Inst.,* vol. 12:C02028, 2017.

[30] A. M. Grant and C. S. Levin, "A new dual threshold time-over-threshold circuit for fast timing in PET," *Phys. Med. Biol.,* vol. 59, no. 13, p. 3421–3430, 2014.

[31] K. Shimazoe, H. Takahashi, B. Shi, T. Orita, *et al.*, "Dynamic Time Over Threshold Method," *IEEE Trans. Nucl. Sci.,* vol. 59, no. 6, pp. 3213-3217, 2012.

[32] W. Yonggang, C. Xinyi, L. Deng, Z. Wensong and L. Chong, "A Linear Time-Over-Threshold Digitizing Scheme and Its 64-channel DAQ Prototype Design on FPGA for a Continuous Crystal PET Detector," *IEEE Trans. Nucl. Sci.,* vol. 61, no. 1, pp. 99-106, 2014.

[33] K. B. Kim, Y. Choi, J. Jung, S. Lee, *et al.*, "Analog and digital signal processing method using multi-time-over-threshold and FPGA for PET," *Med. Phys.,* vol. 45, no. 9, pp. 4104-4111, 2018.

[34] T. Orita, A. Koyama, M. Yoshino, K. Kamada, *et al.*, "The current mode Time-over-Threshold ASIC for a MPPC module in a TOF-PET system," *Nucl. Inst. Meth. Phys. Res. A.,* vol. 912, pp. 303-308, 2018.

[35] M. Uenomachi, T. Orita, K. Shimazoe, H. Takahashi, *et al.*, "Development of slew-rate-limited time-over-threshold (ToT) ASIC for a multi-channel silicon-based ion detector," *J. Inst,* vol. 13:C01040, 2018.

[36] D. Bailey, J. Karp and S. Surti, "Physics and instrumentation in PET," in *Positron Emission Tomography: Basic Science and Clinical Practice*, Springer-Verlag, 2003, pp. 41-67.

[37] G. F. Knoll, "Radiation Sources," in *Radiation Detection and Measurement*, John Wiley & Sons, 2010, pp. 1-28.

[38] G. Saha, "Radioactive decay and interaction of radiation with matter," in *Basics of*

PET Imaging: Physics, Chemistry, and Regulations, Springer Science + Business Media, 2010, pp. 1-17.

[39] S. Cherry, J. Sorenson and M. Phelps, "Modes of radioactive decay," in *Physics in Nuclear Medicine*, Elsevier Saunders, 2012, pp. 19-30.

[40] J. R. Lamarsh and A. J. Baratta, "Atomic and Nuclear Physics," in *Introduction to Nuclear Engineering*, New Jersey, Prentice-Hall, 2001, pp. 5-51.

[41] S. Navalkissoor and A. Grossman, "Targeted Alpha Particle Therapy for Neuroendocrine Tumours: The Next Generation of Peptide Receptor Radionuclide Therapy," *Neuroendocrinology,* vol. 108, p. 256–264, 2019.

[42] N. Tafreshi, M. Doligalski, C. Tichacek, D. Pandya, *et al.*, "Development of Targeted Alpha Particle Therapy for Solid Tumors," *Molecules,* vol. 24, no. 4314, 2019.

[43] S. Fukushima, T. Inoue, T. Inoue and S. Ozeki, "Postoperative irradiation of pterygium with ^{90}Sr eye applicator," *Int. J. Radiat. Oncol. Biol. Phys.,* vol. 43, no. 3, pp. 597-600, 1999.

[44] F. Isohashi, T. Inoue, S. Xing, C. B. Eren, *et al.*, "Postoperative irradiation for pterygium: retrospective analysis of 1,253 patients from the Osaka University Hospital," *Strahlenther Onkol.,* vol. 182, no. 8, pp. 437-442, 2006.

[45] R. Chakravarty, U. Pandey, R. B. Manolkar, A. Dash, *et al.*, "Development of an electrochemical ^{90}Sr–^{90}Y generator for separation of ^{90}Y suitable for targeted therapy," *Nucl. Med. Biol.,* vol. 35, no. 2, pp. 245-253, 2008.

[46] A.M.Ali, J. Thariat, R.-J. Bensadoun, A. Thyss, *et al.*, "The role of radiotherapy in the treatment of pterygium: A review of the literature including more than 6000 treated lesions," *Cancer Radiother.*, vol. 15, no. 2, pp. 140-147, 2011.

[47] J. R. Lamarsh and A. J. Baratta, "Interaction of Radiation with Matter," in *Introduction to Nuclear Engineering*, New Jersey, Prentice-Hall, 2001, pp. 52-116.

[48] G. Knoll, "Radiation interactions," in *Radiation Detection and Measurement*, Wiley, 2010, pp. 29-63.

[49] S. Cherry, J. Sorenson and M. Phelps, "Interaction of Radiation with Matter," in *Physics in Nuclear Medicine*, Elsevier Saunders, 2012, pp. 63-106.

[50] J. R. Richter, B. B. Kasten and K. R. Zinn, "Imaging and Adenoviral Gene Therapy," in *Adenoviral Vectors for Gene Therapy*, Elsevier Academic Press, 2016, pp. 767-802.

[51] S. R. Cherry, J. A. Sorenson and M. E. Phelps, "What is Nuclear Medicine," in *Physics in Nuclear Medicine*, Elsevier Saunders, 20112, pp. 1-6.

[52] H. Anger, "Use of a Gamma-Ray Pinhole Camera for in vivo Studies," *Nature,* vol. 170, pp. 200-201, 1952.

[53] D. E. Copeland and E. W. Benjamin, "Pinhole camera for gamma-ray sources," *Nucleonics,* vol. 5, no. 2, pp. 44-49, 1949.

[54] B. F. Hutton, "The Origins of SPECT and SPECT/CT," *Eur. J. Nucl. Med. Mol. Imaging,* vol. 41 : Suppl 1, pp. S3-16, 2014.

[55] D. Bailey and T. Jones, "Historical development of functional in vivo studies using positron-emitting tracers," in *Positron Emission Tomography: Basic Science and Clinical Practice*, Springer-Verlag, 2003, pp. 3-40.

[56] D. A. Rich, "A Brief History of Positron Emission Tomography," *J. Nucl. Med. Technol.,* vol. 25, pp. 4-11, 1997.

[57] M. Uenomachi, Y. Mizumachi, Y. Yoshihara, H. Takahashi, *et al.*, "Double photon emission coincidence imaging with GAGG-SiPM Compton camera," *Nucl. Inst. Meth. Phys. Res. A.,* vol. 954:161682, 2020.

[58] S. R. Cherry, J. A. Sorenson and M. E. Phelps, "The Gamma Camera: Basic Principles," in *Physics in Nuclear Medicine*, Elsevier Saunders, 2012, pp. 195-208.

[59] K. Blazek, F. D. Notaristefani, P. Maly, R. Pani, *et al.*, "YAP Multi-Crystal Gamma Camera Prototype," *IEEE Trans. Nucl. Sci.,* vol. 42, no. 5, pp. 1474-1482, 1995.

[60] R. Pani, R. Pellegrini, F. Scopinaro, A. Soluri, *et al.*, "Scintillating array gamma camera for clinical use," *Nucl. Inst. Meth. Phsy. Res. A.,* vol. 392, pp. 295-298,

1997.

[61] S. Cherry, J. Sorenson and M. Phelps, "The Gamma Camera: Performance Characteristics," in *Physics in Nuclear Medicine*, Elsevier Saunders, 2012, pp. 208-231.

[62] P. Russo, F. D. Lillo, V. Corvino, P. M. Frallicciardil, *et al.*, "CdTe compact gamma camera for coded aperture imaging in radioguided," *Physica Medica,* vol. 69, pp. 223-232, 2020.

[63] H. Schirrmeister and C. Arslandemir, "Diagnosis of Skeletal Metastases in Malignant Extraskeletal Cancers," *Bone Cancer,* pp. 283-294, 2010.

[64] S. Sato, J. Kataoka, J. Kotoku, M. Taki, *et al.*, "First application of the super-resolution imaging technique using a Compton camera," *Nucl. Inst. Meth. Phys. Res. A.,* vol. 969 : 164034, 2020.

[65] L. Shepp and Y. Vardi, "Maximum likelihood reconstruction for emission tomography," *IEEE Trans. Med. Imag.,* vol. 1, no. 2, pp. 113-122, 1982.

[66] H. Hudson and R. Larkin, "Accelerated image reconstruction using ordered subsets of projection data," *IEEE Trans. Med. Imag.,* vol. 13, no. 4, pp. 601-609, 1994.

[67] S. Cherry, J. Sorenson and M. Phelps, "Tomographic Reconstruction in Nuclear Medicine," in *Physics in Nuclear Medicine*, Elsevier Saunders, 2012, pp. 253-277.

[68] W. Rogers, N. Clinthorne, L. Shao, P. Chiao, *et al.*, "SPRINT II: a second generation single photon ring tomograph," *IEEE Trans. Med. Imag.,* vol. 7, no. 4, pp. 291-297, 1988.

[69] S. Cherry, J. Sorenson and M. Phelps, "Single Photon Emission Computed Tomography," in *Physics in Nuclear Medicine*, Elsevier Saunders, 2012, pp. 279-306.

[70] O. Klemperer, "On the annihilation radiation of the positron," *Math. Proc. Cambridge,* vol. 30, no. 3, pp. 347-354, 1934.

[71] F. Wrenn, M. Good and P. handler, "The use of positron-emitting radioisotopes for

the localization of brain tumors," *Science,* vol. 113 , no. 2940 , pp. 525-527, 1951.

[72] C. Tobias, J. Lawrence, F. Roughton, W. Root and M. Gregersen, "The elimination of carbon monoxide from the body with reference to the possible conversion of CO to CO2," *Am. J. Physiol.,* vol. 145, no. 2, pp. 253-263, 1945.

[73] J. Mitchel, "Applications of recent advances in nuclear physics to medicine; with special reference to the pile and the cyclotron as sources of radioactive isotopes," *Br. J. Radiol.,* vol. 19, no. 228, pp. 481-487, 1946.

[74] H. Wagner, "A brief history of positron emission tomography (PET)," *Semin. Nucl. Med.,* vol. 28, no. 3, pp. 213-220, 1998.

[75] S. Rankowitz, J. Robertson, W. Higinbotham and M. Rosenblum, "Positron Scanner for Locating Brain Tumors," *IRE Int. Conv. Rec.,* 1962.

[76] J. Torres, R. García, A. Aguilar, J. Soret, *et al.*, "Implementation of TOF-PET systems on advanced reconfigurable logic devices," in *Positron Emission Tomography - Recent Developments in Instrumentation, Research and Clinical Oncological Practice*, InTech open access, 2013, pp. 3-30.

[77] M. Ter-Pogossian, D. Ficke, M. Yamamoto and J. Hood, "Super PETT I: a positron emission Tomograph Utilizing Photon Time-of-Flight Information," *IEEE Trans. Med. Imag.,* vol. 1, no. 3, pp. 179-187, 1982.

[78] T. Jones and P. Price, "Development and experimental medicine applications of PET in oncology: a historical perspective," *Lancet Oncol.,* vol. 13, no. 3, pp. e116-e125, 2012.

[79] G. Di Chiro, R. DeLaPaz, R. Brooks, L. Sokoloff, *et al.*, "Glucose utilization of cerebral gliomas measured by [18F] fluorodeoxyglucose and positron emission tomography," *Neurology,* vol. 32, no. 12, pp. 1323-1329, 1982.

[80] E. Browne, e. al., C. edited by Lederer and V. Shirley, in *Table of Isotopes*, New York, Wiley, 1978, p. 516–523.

[81] G. Saha, "Cyclotron and production of PET radionuclides," in *Basics of PET Imaging: Physics, Chemistry, and Regulations*, Springer Science + Business Media, 2010, pp. 131-150.

[82] G. Saha, "Synthesis of PET radiopharmaceuticals," in *Basics of PET Imaging: Physics, Chemistry, and Regulations*, Springer Science + Business Media, 2010, pp. 131-150.

[83] S. Cherry, J. Sorenson and M. Phelps, "Radionuclide and radiopharmaceutical production," in *Physics in Nuclear Medicine*, Elsevier Saunders, 2012, pp. 43-61.

[84] S. Cherry, J. Sorenson and M. Phelps, "Radiation detectors," in *Physics in Nuclear Medicine*, Elsevier Saunders, 2012, pp. 87-106.

[85] G. Knoll, "Scintillation detector principles," in *Radiation Detection and Measurement*, Wiley, 2010, pp. 223-274.

[86] M. Weber, "Inorganic scintillators: today and tomorrow," *J. Lumin,* vol. 100, no. 1-4, pp. 35-45, 2002.

[87] Z. Cho and M. Farukhi, "Bismuth germanate as a potential scintillation detector in positron cameras," *J. Nucl. Med.,* vol. 18, no. 8, pp. 840-844, 1977.

[88] C. Melcher, "Scintillation crystals for PET," *J. Nucl. Med.,* vol. 41, no. 6, pp. 1051-1055, 2000.

[89] M. Casey, "A multicrystal two dimensional BGO detector system for positron emission tomography," *IEEE Trans. Nucl. Sci.,* vol. 33, no. 1, pp. 460-463, 1986.

[90] C. Melcher and J. Schweitzer, "A promising new scintillator: cerium-doped lutetium oxyorthosilicate," *Nucl. Instr. Meth. Phys. Res. A,* vol. 314, no. 1, pp. 212-214, 1992.

[91] K. Shah, J. Glodo, M. Klugerman, W. Moses, *et al.*, "LaBr3:Ce scintillators for gamma ray spectroscopy," *IEEE Nucl. Sci. Conf. Rec.,* vol. 1, pp. 92-95, 2002.

[92] D. Cooke, K. McClellan, B. Bennett, J. Roper, *et al.*, "Crystal growth and optical characterization of cerium-doped Lu1.8Y0.2SiO5," *AIP J. Appl. Phys.,* vol. 88, no. 12, pp. 7360-7362, 2000.

[93] G. Saha, "PET scanning system," in *Basics of PET Imaging: Physics, Chemistry, and Regulations*, Springer Science + Business Media, 2010, pp. 19-39.

[94] J. Y. Yeom, S. Yamamoto, S. Derenzo, V. Spanoudaki, *et al.*, "First performance results of Ce:GAGG scintillation crystals with silicon photomultipliers," *IEEE Trans. Nucl. Sci.,* vol. 60, no. 2, pp. 988-992, 2013.

[95] "BGO, LYSO, and GSO crystal scintillators," Omega Peizo Technologies Inc., [Online]. Available: http://www.omegapiezo.com/crystal_scintillators.html.

[96] "crytur.com | scintillation materials data," CRYTUR, spol. s r.o., [Online]. Available: http://www.crytur.cz/pages/33/crytur-materials.

[97] Furukawa Denshi Co. Ltd., [Online]. Available: http://www.furukawa-denshi.co.jp/cgi-bin/pdfdata/20140428162950.pdf.

[98] A. Karimian and C. Thompson, "Assessment of a new scintillation crystal (LaBr3) in PET scanners using Monte Carlo method," *Nukleonika,* vol. 53, no. 1, pp. 3-6, 2008.

[99] M. Globus and B. Grinyov, "Scintillation detectors for medical and biology applications: materials, design and light collection conditions," in *Radiation Detectors for Medical Applications*, Springer, 2006, pp. 209-242.

[100] A. Fedorov, M. Korzhik, A. Lobko and O. Missevitch, "Novel Fast-Acting Scintillation Detectors for Wide Energy Range Applications," in *Advanced Radiation Sources and Applications*, Springer, 2005, pp. 319-328.

[101] S. David, M. Georgiou, E. Fysikopoulos and G. Loudos, "Evaluation of a SiPM array coupled to a Gd3Al2Ga3O12:Ce (GAGG:Ce) discrete scintillator," *Physica Medica,* vol.31, no. 7, pp. 763-766, 2015.

[102] C. van Eijk, "Inorganic scintillators in medical imaging," *Phys. Med. Biol.,* vol. 47, no. 8, pp. R85-R106, 2002.

[103] I. Vilardi, A. Braem, E. Chesi, F. Ciocia, *et al*., "Optimization of the effective light attenuation length of YAP:Ce and LYSO:Ce crystals for a novel geometrical PET concept," *Nucl. Inst. Meth. Phys. Res. A,* vol. 564, no. 1, pp. 506-514, 2006.

[104] M. Balcerzyk, M. Moszynski, M. Kapusta and M. Szawlowski, "Timing properties of LuAP:Ce studied with aarge-area avalanche photodiodes," *IEEE Trans. Nucl. Sci.,* vol. 48, no. 6, pp. 2344-2347, 2001.

[105] W. Chewpraditkul, L. Swiderski, M. Moszynski, T. Szczesniak, *et al*., "Scintillation Properties of LuAG:Ce, YAG:Ce and LYSO:Ce Crystals for Gamma-Ray Detection," *IEEE Trans. Nucl. Sci.,* vol. 56, no. 6, pp. 3800-3805, 2009.

[106] K. Kamada, T. Yanagida, T. Endo, K. Tsutumi, *et al*., "2 inch diameter single crystal growth and scintillation properties of Ce:Gd3Al2Ga3O12," *J. Cryst. Growth,* vol. 352, no. 1, pp. 88-90, 2012.

[107] G. Knoll, "Photomultiplier tubes and photodiodes," in *Radiation Detection and Measurement*, Wiley, 2010, pp. 275-320.

[108] G. Saha, "Performance characteristics of PET scanners," in *Basics of PET Imaging: Physics, Chemistry, and Regulations*, Springer Science + Business Media, 2010, pp. 97-116.

[109] S. Cherry, J. Sorenson and M. Phelps, "Positron emission tomography," in *Physics in Nuclear Medicine*, Elsevier Saunders, 2012, pp. 307-343.

[110] G. Saha, "Data acquisition and correction," in *Basics of PET Imaging: Physics, Chemistry, and Regulations*, Springer Science + Business Media, 2010, pp. 41-69.

[111] D. Bailey, "Data acquisition and performance characterization in PET," in *Positron Emission Tomography: Basic Science and Clinical Practice*, Springer-Verlag, 2003, pp. 69-90.

[112] M. Defrise, P. Kinahan and C. Michel, "Image reconstruction algorithms in PET," in *Positron Emission Tomography: Basic Science and Clinical Practice*, Springer-Verlag, 2003, pp. 91-114.

[113] M. Ter-Pogossian, M. Phelps, E. Hoffman and N. Mullani, "A positron-emission transaxial tomograph for nuclear imaging (PETT)," *Radiology,* vol. 114, no. 1, pp. 89-98, 1975.

[114] M. Phelps, E. Hoffman, N. Mullani and M. Ter-Pogossian, "Application of annihilation coincidence detection to transaxial reconstruction tomography," *J. Nucl. Med.,* vol. 16, no. 3, pp. 210-224, 1975.

[115] C. S. Levin and E. J. Hoffman, "Calculation of positron range and its effect on the

fundamental limit of positron emission tomography system spatial resolution," *Phys. Med. Biol.,* vol. 44, p. 781–799, 1999.

[116] H. Alva-Sánchez, C. Quintana-Bautista, A. Martínez-Dávalos, M. A. Ávila-Rodríguez and M. Rodríguez-Villafuerte, "Positron range in tissue-equivalent materials: experimental microPET studies," *Phys. Med. Biol.,* vol. 61, p. 6307–6321, 2016.

[117] S. Cherry, J. Sorenson and M. Phelps, "Electronic Instrumentation for Radiation Detection Systems," in *Physics in Nuclear Medicine*, Elsevier Saunders, 2012, pp. 107-124.

[118] "Readout Methods for Arrays of Silicon Photomultipliers," Semiconductor Components Industries, LLC, 2014.

[119] A. L. Goertzen, X. Zhang, M. M. McClarty, E. J. Berg, *et al.*, "Design and Performance of a Resistor Multiplexing Readout Circuit for a SiPM Detector," *IEEE Trans. Nucl. Sci,* vol. 60, no. 30, pp. 1541-1549, 2013.

[120] H. Anger, "Scintillation Camera," *Rev. Scientific Inst.,* vol. 29, pp. 27-33, 1958.

[121] Y. Shao, "A new timing model for calculating the intrinsic timing resolution of a scintillator detector," *Phys. Med. Biol.,* vol. 52, no. 4, pp. 1103-1117, 2007.

[122] E. Auffray, B. Frisch, F. Geraci, A. Ghezzi, *et al.*, "A comprehensive & systematic study of coincidence time resolution and light yield using scintillators of different size, wrapping and doping," *IEEE Nucl. Sci. Conf. Rec.,* pp. 64-71, 2011.

[123] K. Kamada, P. Prusa, M. Nikl, C. Piemonte, *et al.*, "2-inch size crystal growth of Ce:Gd3Al2Ga3O12 with various Ce concentration and their scintillation properties," *IEEE NSS/MIC,* pp. 1698-1701, 2012.

[124] K. Kamada, M. Nikl, S. Kurosawa, A. Beitlerova, *et al.*, "Alkali earth co-doping effects on luminescence and scintillation properties of Ce doped Gd3Al2Ga3O12 scintillator," *Opt. Mater.,* vol. 41, pp. 63-66, 2015.

[125] Z. Gu, R. Taschereau, N. T. Vu, D. L. Prout, *et al.*, "Performance evaluation of HiPET, a high sensitivity and high resolution preclinical PET tomograph," *Phys. Med. Biol.,* vol. 65, no. 4:5009, 2020.

[126] S. Gundacker, A. Knapitsch, E. Auffray, P. Jarron, *et al.*, "Time resolution deterioration with increasing crystal length in a TOF-PET system," *Nucl. Inst. Meth. Phys. Res. A,* pp. 92-100, 2014.

[127] W. Yonggang, D. Junwei, Z. Zhonghui, Y. Yang, *et al.*, "FPGA Based Electronics for PET Detector Modules With Neural Network Position Estimators," *IEEE. Trans. Nucl. Sci.,* vol. 58, no. 1, pp. 34-42, 2011.

[128] Y. Wang, W. Zhu, X. Cheng and D. Li, "3D position estimation using an artificial neural network for a continuous scintillator PET detector," *Phys. Med. Biol.,* vol. 58, p. 1375–1390, 2013.

[129] S. Delorme, R.Frei, C. Joseph, J.-F. Loude and C. Morel, "Use of a neural network to exploit light division in a triangular scintillating crystal," *Nucl. Inst. Meth. Phys. Res. A.,* vol. 373, no. 1, pp. 111-118, 1996.

[130] R. F. D. Clement, J.-F. Loude and C. Morel, "Development of a 3D Position Sensitive Scintillation Detector using Neural Networks," *IEEE NSS/MIC,* vol. 3, pp. 1448-1452, 1998.

[131] J. Schmal, S. Surti and J. Karp, "Characterization of stacked-crystal PET detector designs for measurement of both TOF and DOI," *Phys. Med. Biol.,* vol. 60, no. 9, pp. 3549-3565, 2015.

[132] D. H. Wilkinson, "The Phoswich—A Multiple Phosphor," *Rev. Scientific Inst.,* vol. 23, no. 8, pp. 414-417, 1952.

[133] M. Dahlbom, L. MacDonald, L. Eriksson, M. Paulus, *et al.*, "Performance of a YSO/LSO phoswich detector for use in a PET/SPECT system," *IEEE Trans. Nucl. Sci.,* vol. 44, no. 3, pp. 1114-1119, 1997.

[134] V. Nagarkar, V. Gaysinskiy, V. Gelfandbein, S. Miller, *et al.*, "Continuous Phoswich™ detector for molecular imaging," *IEEE Nucl. Sci. Conf. Rec.,* pp. 4-9, 2010.

[135] T. Tsuda, H. Murayama, K. Kitamura, N. Inadama, *et al.*, "Performance evaluation of a subset of a four-layer LSO detector for a small animal DOI PET scanner: jPET-RD," *IEEE Trans. Nucl. Sci.,* vol. 53, no. 1, pp. 35-39, 2006.

[136] A. Choghadi, K. Shimazoe and H. Takahashi, "New DOI Identification Approach for HighResolution PET Detectors," *JPS Conf. Proc.,* vol. 11:060002, 2016.

[137] K. Shimazoe, A. Choghadi, H. Takahashi and K. Watanabe, "Single Side Readout Depth of Interaction Method With Wavelength Discrimination," *IEEE Trans. Nucl. Sci.,* vol. 63, no. 2, pp. 679-684, 2016.

[138] S. Ren, Y. Yang and S. R. Cherry, "Effects of reflector and crystal surface on the performance of a depth-encoding PET detector with dual-ended readout," *Med. Phys.,* vol. 41:072503, 2014.

[139] Z. Kuang, X. Wang, C. Li, X. Deng, *et al*., "Performance of a high-resolution depth encoding PET detector using barium sulfate reflector," *Phys. Med. Biol.,* vol. 62, p. 5945–5958, 2017.

[140] Y. Shao, K. Meadors, R. W. Silverman, R. Farrell, *et al*., "Dual APD Array Readout of LSO Crystals: Optimization of Crystal Surface Treatment," *IEEE Trans. Nucl. Sci.,* vol. 49, no. 3, pp. 649-654, 2002.

[141] K. C. Burr, A. Ivan, D. E. Castleberry, J. W. LeBlanc, *et al*., "Evaluation of a Prototype Small-Animal PET Detector With Depth-of-Interaction Encoding," *IEEE Trans. Nucl. Sci.,* vol. 51, no. 4, pp. 1791-1798, 2004.

[142] F. ur-Rahman, Y.-C. Tai and A. L. Goertzen, "Use of systematic surface roughing to enhance the spatial resolution of the dual-ended readout of axially-oriented 100 mm long LYSO crystals," *Phys. Med. Biol.,* vol. 57, pp. N501-N512, 2012.

[143] A. Sanaat and H. Zaidi, "Depth of Interaction Estimation in a Preclinical PET Scanner Equipped with Monolithic Crystals Coupled to SiPMs Using a Deep Neural Network," *Appl. Sci.,* vol. 10, no. 4753, 2020.

[144] A. Dhal, G. Mukherjee, M. Bhattacharjee, V. Naik, *e. al*., "Decay measurements of 43K($\beta-$)43Ca by HRS and TAS," *EPJ WEB CONF,* vol. 146, p. 10013, 2017.

[145] T. Burrows, "Nuclear Data Sheets for A = 48," *Nucl Data Sheets,* vol. 107, no. 7, p. 1747–1922, 2006.

[146] U. Schötzig, H. Schrader, E. Schönfeld, E. Günther and R. Klein, ", Standardisation and decay data of 177Lu and 188Re,," *Appl. Radiat. Isot.,* vol. 55,

no. 1, p. 89–96, 2001.

[147] M. Melis, E. Vegt, M. Konijnenberg, M. de Visser, *e. al.*, " Nephrotoxicity in Mice After Repeated Imaging Using 111In-Labeled Peptides," *J. Nucl. Med.,* vol. 51, no. 6, p. 973–977, 2010.

[148] S. Missault, L. Peeters, H. Amhaoul, D. Thomae *e. al*., "Decreased levels of active uPA and KLK8 as-sessed by [111In]MICA-401 binding correlate with the seizure burden in an animal model of temporal lobe epilepsy," *Epilepsia, ,* vol. 58, p. 1615–1625, 2017.